Relating Multi-Scale Plume Detection and Area Estimates of Methane Emissions: A Theoretical and Empirical Analysis

Sudhanshu Pandey,*,† John Worden,† Daniel H. Cusworth,‡ Daniel J. Varon,¶ Matthew D. Thill,† Daniel J. Jacob,¶ and Kevin W. Bowman†

†*Jet Propulsion Laboratory, California Institute of Technology, Pasadena, CA, USA*

‡*Carbon Mapper, Inc., Pasadena, CA, USA*

¶*School of Engineering and Applied Sciences, Harvard University, Cambridge, MA, USA*

E-mail: sudhanshu.pandey@jpl.nasa.gov

Abstract

Methodologies for inferring surface emissions of atmospheric trace gases can be categorized into plume detection and area-scale estimation. Plume detections are observations of emissions from either individual or clustered point sources. Area estimates are derived from top-down atmospheric flux inversion models or bottom-up inventories, which infer mean emissions typically over spatial scales greater than 10 km and temporal scales greater than a week. Integrating information from these distinct methodologies can enhance our understanding of emission sources and improve emission monitoring. However, such integration is challenging because plume-detecting instruments exhibit irregular and infrequent sampling, as well as varying detection sensitivities and spatial footprint sizes. This study presents a theoretical framework to relate plume and area

estimates in dense point-source emission fields. We show that the spatial footprint size of plume-detecting instruments impacts the emission rate distribution of plumes. We find a robust linear relationship in empirical tests between the sums of gridded plume emission rates and area estimates for the Permian Basin's oil and gas emissions. After accounting for the plume detectors' sampling of the Permian emission field, the weekly plume sums demonstrate a strong correlation with TROPOMI top-down area estimates ($R^2 > 0.94, P < 0.005$). We assess the feasibility of using plume data to inform area estimates within a Bayesian assimilation framework. We perform two plume inversions using prior area estimates from (1) constant EDF bottom-up inventory and (2) weekly-updated TROPOMI inversion estimates. We find that the posterior estimate of the EDF plume inversion improves, bringing it in good agreement with independent TROPOMI estimates. In the TROPOMI plume inversion, area estimates' fine spatial resolution features improve. Our analysis underscores that plume datasets obtained from aircraft, satellites, and in situ instruments can evaluate and improve area estimates in dense point source emission fields.

1 Introduction

Understanding methane emissions is crucial for developing climate change mitigation strategies and predicting future climate. New observational techniques to detect methane plumes from point sources have significantly advanced our understanding of methane emissions [1–12]. Reducing methane emissions, especially from large point sources (often called super-emitters), which often constitute a large fraction of total emissions, is now central to climate change mitigation efforts [13–15]. Plumes are detected over a wide range of spatial scales (1 m to 10 km) but are limited to temporal snapshots of the emissions from a single point source or a cluster of point sources ($<$ 1 hour). An area-scale observing system provides area-average estimates of emissions by aggregating emissions at spatial ($>$ 10 km) and temporal (>weekly) grid cells. Area estimates sacrifice spatial resolution of emissions estimates to improve the precision of the magnitude of emission estimates. In this paper, we present a theory to relate the sum of plume detections to area emissions estimates over a region of dense point source emissions. We empirically test our theory using data on the Permian oil and gas sector emissions. In turn, we demonstrate novel applications of plumes as tools for evaluating and informing area estimates in a dense emission field.

Area estimates of emissions are derived from bottom-up approaches [16,17] and top-down flux inversions [18–24]. Bottom-up inventories quantify emissions by extrapolating emission factors (e.g., emission per wellhead) with emission activity (e.g., number of wellheads). However, emission factors vary across operating conditions, leading to substantial inaccuracies in emission estimates. Top-down approaches quantify emissions by comparing atmospheric chemical transport model (CTM) simulations with observed atmospheric concentration gradients caused by those emissions. The diffusive and chaotic nature of atmospheric transport, the computational cost of CTM simulations, and observation coverage limit the spatial resolution of top-down area estimates [25–29]. Evaluating the accuracy of flux inversion emission estimates poses several challenges. These inversions constrain total emissions from various sources across large areas. Their posterior estimates are evaluated against atmospheric con-

centration measurements from in situ and TCCON sites, using a CTM to simulate emissions. However, CTM errors are a major component of the overall flux inversion errors[25–27]. Therefore, a CTM-based evaluation method may be insensitive to the CTM-related errors in the flux inversion estimates.

Plume detectors exploit sharp enhancements in a methane concentration field generated from a single point source or cluster of point sources. In situ plume-detecting instruments can be mounted on the ground, automobile, or aircraft. Column-observing plume instruments are typically deployed onboard aircraft or satellites. These remote sensing instruments can be either active (e.g., LIDAR instruments;[30]) or passive (e.g., GHGSat, Sentinel-2, PRISMA, Carbon Mapper, MethaneSAT;[31–34]). Emissions spatial resolution is an emission-observing system's ability to pinpoint the emissions' location. The emission spatial resolution of plumes is better than area estimates, which facilitates rapid action and mitigation of leaks or other fixable processes causing emissions. Plume detections are used for Leak Detection and Repair (LDAR) techniques, focusing on fixing anomalous methane emitters for mitigation efforts. Observed plumes can account for a large fraction of the emission *rate* [kg hr^{-1}] in certain sectors, providing an advantage for targeted mitigation efforts[30,35,36]. Efforts to generate regional and national inventories that account for the large point source emissions absent in traditional bottom-up inventories have been undertaken by a few studies[8,37–39]. These studies extrapolate plume detections from measured facilities under some assumption of temporal persistence in the emissions. Some studies have also used plume detections to improve the prior emissions in the flux inversion estimates[40]. The distribution of plume emission rates also sheds light on emission mechanisms, pointing to opportunities for effective mitigation by addressing the contributions of large emitters to total emissions[30,35].

Because area estimates quantify the total emissions from a single sector or many sectors together, they are straightforwardly related to regional total emissions. Plume detections are advantageous for identifying large emissions from point sources, but their relation to regional total emissions remains complex for the following reasons. First, the spatial specificity of

plumes varies by orders of magnitude among the plume-detecting instruments of different footprint sizes: $1-20$ m emission spatial resolution for hand-held Optical Gas Imaging (OGI) cameras as well as ground and aerial in situ instruments[6,41–44], $10-150$ m for aerial imaging instruments[3,32,35,45,46], and 50 — 1000 m for satellite imaging instruments[7,31,33,34,47–53]. The TROPOspheric Monitoring Instrument (TROPOMI) methane retrievals, which are originally used for providing top-down constraint in flux inversions, also observe point sources at a footprint size of roughly 7 km[7,48,49,51,54–56]. Second, the detection sensitivity also varies significantly among plume instruments. For instance, Sentinel-2, a multi-band instrument with a 20-m footprint utilizing only two data points from the observation day, can detect >1 t hr^{-1} point sources[34]. GHGSat, with a similar spatial footprint, can detect plumes with emission rates even below 100 kg hr^{-1} in favorable observation conditions[30,57,58]. Third, plumes can account for a large fraction of the total emission rate [kg hr^{-1}] of a region for some sectors, but the detected mass enhancement in plumes is only a tiny mass [kg] fraction of total emissions. For instance, an aircraft campaign samples the emissions field of a region for tens of hours over a year, observing a very small mass fraction of the monthly or annual emissions. It can be assumed that the plumes are a significant mass fraction of emissions if they represent persistent sources. However, this assumption is not always valid[10,59]. Fourth, intermittent point source emissions can bias temporal mean emission estimates. Both in situ and passive total column imaging instruments tend to observe methane concentrations in the late morning or afternoon to detect point sources or facility emissions. In situ instruments prefer a well-developed planetary boundary layer, and passive imaging instruments prefer strong solar backscatter light. For example, the diurnal cycle of oil and gas emissions can be strong due to daytime maintenance operations[59,60]. As a consequence, emission inferences from exclusively afternoon data can bias temporally averaged emissions.

In order to address these issues, we present a theory (Section 2) to connect plume detections and area estimates of dense point source emission fields. We derive a statistical relation between plume sums and area estimates, considering instrument detection sensitivity, sam-

pling, and the periodicity of emissions. In Section 3, we describe the Permian Basin oil and gas emission datasets used in this study. In Section 4, we test the statistical relationship between plume sums and area estimates using the Permian data. In Section 5, we present approaches to evaluate and inform area emission estimates using plume sums. Thereafter, we discuss our findings in Section 6 and provide a summary in Section 7.

2 Theory

2.1 Definitions

- **Point source**: A source of emission with a small spatial extent, less than a few meters, much smaller than or comparable to the footprint size of any plume-observing instrument. Point sources can be infrastructure components that emit plumes of highly concentrated trace gas. The emission rate of a point source has the unit kg hr^{-1}.

- **Plume detection**: The detection of emissions from a single point source or a cluster of point sources, observed as a group of concentration-enhanced footprint pixels by an imaging instrument. In-situ instruments also detect plumes as a sharp enhancement in concentrations downwind of one or more point sources. The emission rate of a plume is given in the unit of kg hr^{-1}.

- **Area estimates**: Estimates of total emissions over a large spatial ($>$ 10 km) and temporal ($>$ week) interval for a sector or sum of sectors. Area estimates are derived using top-down flux inversions or bottom-up approaches. An area estimate of emissions has the unit kg hr^{-1} m^{-2}.

Emissions from point sources in a dense point source emission field like an oil and gas basin can be observed as both area estimates and plume detections but with different characteristics in terms of spatial resolution and percentage of total emissions observed. Methane plume detections and point sources are sometimes used interchangeably in the literature. A plume

is often assumed to originate from a single point source. We emphasize the importance of the distinction between a point source and a plume detection for our analysis, as a plume can contain emissions from multiple point sources[40,51].

A single plume detection entry in a plume dataset consists of at least three values: (1) source location of the plume in latitude and longitude, (2) time of plume detection, and (3) emission rate with uncertainty estimates. Some plume datasets also provide the wind speed data used for emission rate quantification, as wind is generally considered the main error source in the quantification. Area estimate datasets are typically provided in a gridded format, with each grid cell representing the mean emission rate over a spatial and temporal interval. These grid cells are defined on latitude-longitude coordinates (typically for global or continental-scale inversions) or surface distance coordinates (for regional inversions). Some area estimates include uncertainty quantification or a full error covariance matrix for the emission values[61,62]. The emission values can represent total emissions from a grid cell (typically from top-down inversions) or categorical emissions from sectors (typically from bottom-up inventories such as the EDGAR and EPA inventories[16,63]. Top-down flux inversions sometimes provide sectoral partitioning, but they still rely heavily on bottom-up sector-partitioning information[24,61].

2.2 Effect of Instrument Footprint Size on Plume Detection

We explore here the effects of the spatial footprint size of plume detectors observing a dense point source emission field on the number of possible plume detections and their emission rates.

Consider an observing system monitoring a dense point source emission field in grid cell c, an area of size $l_c \times l_c$ [m^2]. The observing system uses a concentration imaging instrument i with spatial footprint pixels of size $l_i \times l_i$ [m^2]. The observed concentration field is a discrete version of the underlying emission field, with a resolution determined by the instrument's footprint. The instrument identifies a group of enhanced pixels forming a Gaussian plume

shape for a plume detection. A rough criterion for an enhanced pixel is that the pixel's concentration value is at least $2\sigma_i$ higher than the background concentration value, where σ_i is the footprint concentration precision of the instrument. Let the area needed to confidently flag a Gaussian-shaped plume be δ_i^2 [m^2]. We refer to the square root of this area, δ_i [m], as the *emission spatial resolution*. δ_i measures the instrument's spatial specificity or its ability to differentiate emissions from distinct point sources.

For instruments with similar concentration precision, δ_i should demonstrate a roughly linear relationship with l_i. This relationship holds under the assumption that the number of pixels required to detect a plume remains consistent across different scales. However, this assumption does not always apply. For instance, TROPOMI can identify plumes with fewer pixels due to its superior spectral resolution and concentration precision compared to other instruments. To maintain clarity and simplicity in our conceptual exercises (Figures 1 and 2), we assume l_i is linearly dependent on δ_i— doubling l_i doubles δ_i. In practice, δ_i is influenced by additional factors, including instrument concentration precision, wind speed, surface albedo, and spatial distribution of point sources. Therefore, estimating δ_i for an instrument is challenging. Our aim here is not to provide an exact estimate of δ but to underscore its impact on plume aggregation.

Figure 1 shows a snapshot of the column average concentration field of a trace gas from a Weather Research and Forecasting model coupled with Chemistry (WRF-Chem) CTM simulation at 1×1 km^2 resolution with ten point emission sources. We conceptually examine two physical effects on the number of plume detections (N) using this figure: (1) reduction of N due to clustering of plumes from distinct point sources as l_i coarsens and (2) reduction of N as precision noise worsens. We ignore spatially varying systematic measurement errors that could influence detections in this exercise.

Figure 1 shows that increasing l_i from left to right panels causes a clustering of plumes from individual point sources into larger plumes, leading to a reduction in N. The information about the origin of individual plumes from specific point sources is lost, leading to

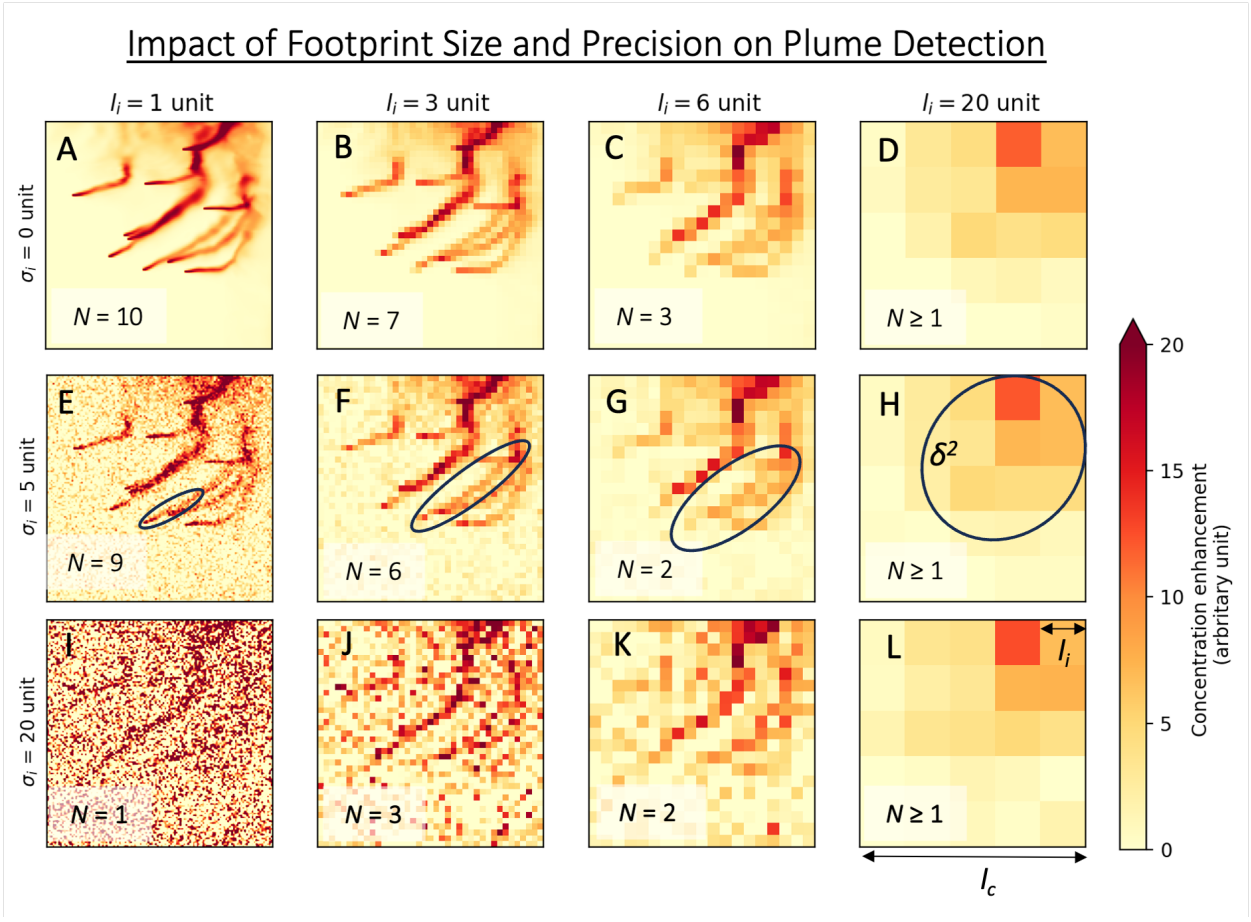

Figure 1: Conceptual illustration of the influence of instrument footprint size l_i and precision error σ_i on plume detection. Panel (A) shows the column average concentration field from a CTM simulation at 1×1 km^2 spatial resolution with plumes from 10 point sources. Each panel represents a coarse (left to right) and/or noisy version (top to bottom) of the same concentration field (Panel A) across the same spatial domain. Random noise with standard deviation σ_i is added to the panels in the leftmost column. The noise reduces due to aggregation across adjacent pixels as the columns progress to the right. The number of plume detections, N, is marked in each panel. The grid cell size (l_c) and instrument pixel size (l_i) are marked in Panel (L). A rough estimate of emission spatial resolution, δ_i, is given by the area ($= \delta_i^2$) of black ellipses marked in the second row. Note that the units are arbitrary, emphasizing the adaptability of the diagram to a wide range of spatial scales and trace gas plumes. While the original WRF-Chem CTM run was performed at 1×1 km spatial resolution, this conceptual illustration can be extended to a wide spatial resolution range (1 m to 10 km). Our determination of N is subjective, as it is in the real world. The values of N depend on the observing system, often including a human decision on the successful plume detection.

a worsening in emission spatial resolution δ_i. If point sources are densely and uniformly distributed, the number of point sources would be proportional to the area, and the δ_i would worsen proportionally to l_i. The merging of plumes increases the emission rates of the remaining, larger plumes. The boosting would also occur when the plume from a large source masks smaller point sources within its area, as the emissions from the small sources will boost the concentration enhancement of the large plume. This boosting implies that the plume emission rates from different footprint size instruments like AVIRIS-NG ($l_i = 5$ m), GHGSat ($l_i = 25$ m), Carbon Mapper - Tanager ($l_i = 30$ m), MethaneSAT ($l_i > 100$ m), and TROPOMI ($l_i > 5$ km) will differ. At very coarse resolutions ($l_i = 20$ km), the instrument's ability to identify individual plumes and their sources is lost (although it is known that at least one source is present). In this case, area emission estimation methods like atmospheric flux inversions and mass balance methods can quantify emissions[40,64–67].

N decreases with increasing precision error σ_i from top to bottom panels in Figure 1. Interestingly, in the bottom-most panel ($\sigma_i = 20$ units), it is possible that more plumes are detected at spatial scales $l_i = 3$ and 6 units than at $l_i = 1$ unit. This effect is observed in the real world. For instance, TROPOMI can detect plumes from large areas like cities or wetlands, but zooming in with fine spatial resolution instruments does not always reveal a fine-scale plume in these scenes, likely due to the dominance of instrument noise over the plume signal at fine spatial scales[56].

2.3 Effect of Instrument Footprint Size on Plume Emission Rate Distribution

A plume instrument's Probability of Detection (POD) function represents the likelihood of detecting a *single* point source plume with a specific emission rate. The POD curve typically has a sigmoid shape (see Figure 2.A): POD approaches 0 for small point emissions or diffused area sources creating weak plumes (the concentration enhancement within a pixel is below the instrument's detection capability) and approaches 1 for large point source emission

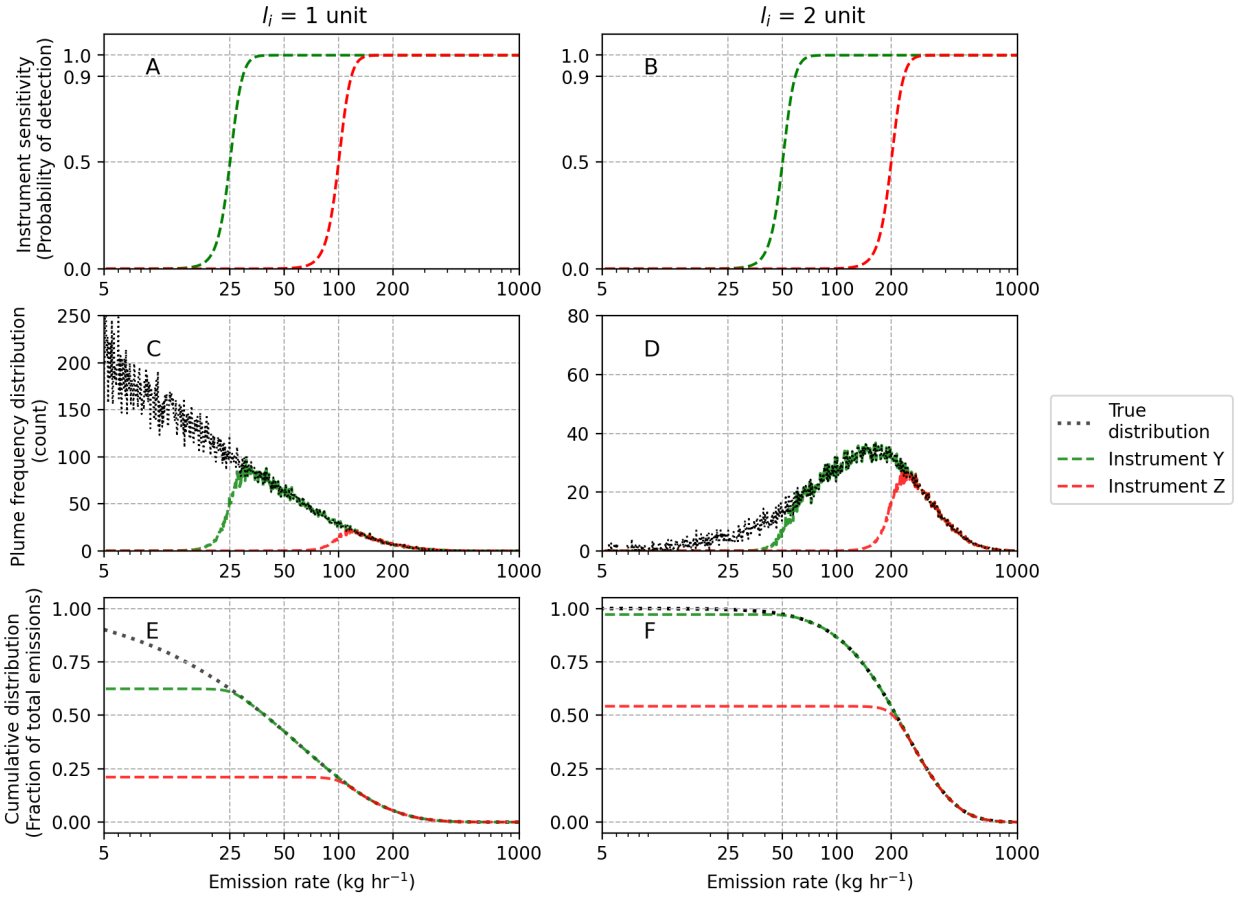

Figure 2: Conceptual illustration of the impact of footprint size on plume emission rate distribution in a hypothetical dense point source emission field. Panel (A) presents the POD curves for two hypothetical instruments, Y and Z (green and red, respectively) with footprint size $l_i = 1$ unit. Panel (B) shows POD changes when aggregating pixels at $l_i = 2$ units. Panel (C) displays the frequency distribution of plume emission rates for $l_i = 1$ unit, with the true distribution in black and observed distributions for the instruments red and green. Panel (D) shows the frequency distributions for $l_i = 2$ units. Panels (E) and (F) show the cumulative fraction of total emissions observed by the two instruments at the two l_i values.

rates. Observation conditions such as surface albedo, wind speed, and the detector's altitude impact POD[57,58]. Surface albedo can modify the instrument's received signal, altering the POD curve. Higher wind speeds may dilute the concentration enhancement of instrument footprint pixels, complicating plume detection.

Figure 2 provides a conceptual illustration of how the spatial resolution of an observing system impacts the detection of plumes according to the POD in a dense point source field. It demonstrates the interplay between precision error and spatial resolution by analyzing the distribution of plume emission rates. For this conceptual illustration, we assume that the point sources are uniformly distributed in the field (under the ergodic assumption), meaning the number of point sources within an area is proportional to the plume area. We use logistic functions for the POD of the hypothetical instruments and Gamma distributions for the hypothetical true point source distribution.

Figure 2.A compares the POD functions for two hypothetical instruments. Let P_{50} [kg hr^{-1}] be the emission rate at which the POD value is 50% (meaning half the plumes at this emission rate will be detected). At $l_i = 1$ unit, the P_{50} of instrument Y (25 kg hr^{-1}) is four times better than that of instrument Z (100 kg hr^{-1}), indicating that instrument Z has four times poorer pixel precision (σ_i) than instrument Y. The middle panels of Figure 2 show the frequency distribution of plume emissions from the $l_i \times l_i$ pixels and the corresponding detection rate for the two instruments (POD curve multiplied by the emission rate distribution).

In the right column panel of the figure, four pixels are aggregated together, resulting in some interesting effects. First, the POD of the instruments worsens by a factor of 2 because aggregating pixels dilutes the enhancement signal of a point source by one-fourth. Although averaging the noise over four pixels reduces the precision error σ_i by a factor of $\sqrt{4}$, the net effect is a worsening of the POD by a factor of 2. Second, the emission signal improves by a factor of 4. A 2x2 pixel group contains four times the point sources compared to a 1x1 pixel, thus increasing the emission signal (the amount of emitted mass per unit time under

a pixel).

As l_i increases, the number of low-emission groups of $l_i \times l_i$ pixels decreases, fundamentally changing the shape of the emission rate distribution. Following the central limit theorem, the shape becomes more bell-shaped when identically and independently distributed (IID) pixel-wise emissions are summed together. The expected values of the distribution shift to the right by a factor $\propto l_i^2$. The bottom panels show the 'true' and observed cumulative emission distributions (normalized integrals of the curves from the middle panels). These panels show the fraction of total emissions represented by plumes detected at or above a given emission rate. Instrument Y can detect nearly 100% of the sum of point source emissions when observing at $l_i = 2$, but only 60% at $l_i = 1$, highlighting the trade-off between spatial specificity and total emission estimation at different l_i.

The conceptual illustration highlights the trade-offs between detection sensitivity and spatial resolution in instruments. Fine spatial resolution instruments observe a lower fraction of total emissions but with good emissions spatial resolution, providing better information on the location of point sources. Conversely, coarse spatial resolution instruments detect a higher fraction of total emissions but with reduced spatial specificity. The conceptual illustration allows for generalization that includes detections by instruments from meter-scale (typically capturing a single-point source) to kilometer-scale resolution (typically capturing emissions from a cluster of point sources). In some sense, an area emission observing system is an extreme case of a coarse spatial resolution system designed to be sensitive to 100% of the total emissions but lacks point source location information.

2.4 Statistical Relation between Area Estimates and Plume Sums

Here, we present a statistical relationship between area estimates of grid cell emissions, representing mean emissions over a spatial and temporal interval, and the sum of plume emission rates within the grid cell. The complete derivation of the relationship is given in Appendix Section A.1. Factors to consider when relating area estimates and plume sums are

as follows. Instruments with different footprint sizes (see Figure 1) or detection sensitivities need to be treated separately in the relation. Furthermore, the extent of sampling of the emission field by the plume instrument needs to be considered because it dictates the number of plume detections and, consequently, the magnitude of plume sums. Potential temporal biases in the sampling of the emission field must also be accounted for.

Consider an emission sector or sub-sector category, s, within a large grid cell c of area l_c^2 [distance^2] composed of densely distributed point sources. The size of l_c^2 can range from something like 25×25 km^2 (a regional flux inversion grid cell) to more than $5^\circ \times 5^\circ$ latitude–longitude (a global flux inversion grid cell). The time interval of c can be between a week and a year, corresponding again to flux inversions.

Suppose a plume instrument i scans different portions of c in a v number of scans within the period of c. From these scans, plume detections are identified, and emission quantification for these plumes is conducted. Let η_{ic} [unitless] be the instrument's *sampling* of the emission field of c by i within the time interval of c. η_{ic} is given by the sum of the ratios of the ground areas of the v scans and the grid cell area l_c^2.

Let y_{ics} [mass time^{-1}] denote the sum of emission rates of the plume detections by i in the spatial and temporal extent of c. Let x_{cs} [mass time^{-1}] be the total emission rate from c of s. The relationship between y_{ics} and the total area estimates x_{cs} is given by:

$$y_{ics} = \tau_{ics}\kappa_{is}\eta_{ic}x_{cs} \tag{1}$$

κ_{is} [unitless] is a *periodicity bias* is the temporal sampling bias of i due to periodic (continuous or intermittent, see Section A.1) emissions from s. τ_{ics} is the *plume factor*. $\tau_{ics} = \frac{y_{ics}}{x_{cs}}$, when $\eta_{ic} = 1$ and $\kappa_{is} = 1$. $\tau_{ics} \in [0, 1]$ is defined as the fraction of the total emissions of s expected to be observable by i in one complete scan of c ($\eta_{ic} = 1$) provided there was no periodicity bias ($\kappa_{is} = 1$). τ is dictated by the instrument plume detection sensitivity or the POD in the observing conditions of c. Note that in our model, y is not directly comparable to x. y can be greater than x depending on the amount of scanning of

the emission field of c. For instance, consider a hypothetical instrument with $\tau\kappa = 1$. It will have $y = x$ for a single complete scan of the grid cell ($\eta = 1$), but if the grid cell is sampled 10 times completely by the instrument during the interval of c, $y = 10x$.

3 Data

We use plume detections and area estimates of oil and gas emissions in the Permian Basin, USA. Detailed descriptions of these datasets are provided in Appendix Section B. We use plume data from the two aircraft instruments (ANG and GAO) of the Carbon Mapper campaign in the fall of 2019[68]. The plume data cover a six-week period from September 24 to November 4, 2019. We utilize the gridded area estimates from two sources: (1) concurrent weekly top-down TROPOMI flux inversions[9] and (2) the annual mean Environmental Defense Fund's (EDF) 2018 bottom-up inventory[69], both with a spatial resolution of $0.25° \times 0.3125°$ latitude and longitude ($\approx 25 \times 25$ km^2).

Figure 3 shows the gridded area emission estimates and the weekly coverage (shown as η) from the two aircraft instruments. ANG and GAO are considered different instruments due to differences in observation configuration and capability (see Section B.2).

η_{ic} represents observation sampling or coverage of the grid cell c by instrument i over the course of a week. The sampling occurred over multiple flight tracks each week. For each flight track j, we use the fraction of a c covered, which is denoted by $I(j, c)$. Under an assumption of homogeneity, we compute η_{ic} by summing these fractions overall flight tracks during the week:

$$\eta_{ic} = \sum_{j} I(j_i, c). \tag{2}$$

The product $\tau_{is}\kappa_{is}$ is estimated by taking the ratio of plume sums to the product of TROPOMI area emission estimates and η, both summed across the Permian:

$$\tau_{is}\kappa_{is} = \frac{\sum_{c\in\text{Permian}} y_{ics}}{\sum_{c\in\text{Permian}} \eta_{ic} x_{cs}} \tag{3}$$

The weekly plume counts, $\tau_{is}\kappa_{is}$, and η_{ic} values of the two instruments are given in Table 1. $\tau_{is}\kappa_{is}$ are used in the plume inversions (Section 5.2) and discussed further in Section 6.

Table 1: Weekly statistics of the plume detections by the ANG and GAO instruments of the Carbon Mapper Fall 2019 Permian survey. # is the number of plume detections per week. η is the weekly sampling of the instruments. $\tau\kappa$ is the plume factor times periodicity bias estimated by taking the ratio between plume sums and area emissions (see Equation 3). $\pm$ denotes one standard deviation spread.

Week	GAO Instrument			ANG Instrument		
	# plumes	$\tau\kappa$	η	# plumes	$\tau\kappa$	η
Sep-27	-	-	-	266	0.68	38.7
Oct-04	-	-	-	318	0.87	22.9
Oct-11	198	1.01	16.9	351	0.7	38.7
Oct-18	187	1.0	20.6	709	0.81	48.6
Oct-25	396	1.05	23.8	310	0.67	29.1
Nov-01	212	0.89	16.7	-	-	-
Mean	250	0.99 $\pm$ 0.06	19.5	402	0.75 $\pm$ 0.08	37.2

4 Empirical Analysis

4.1 Probably Density functions (PDF) of Plume Detections

Figure 4 presents the PDFs of emission rates of weekly plume detections by the ANG and GAO instruments. The two instruments exhibit different PDFs: GAO shows superior plume detection capabilities, identifying more plumes below 30 kg hr^{-1}. The range of the expected value of weekly PDFs for the ANG plume detections is 318–485 kg hr^{-1} (mean = 417 kg hr^{-1}), and for GAO detections, it is 243–443 kg hr^{-1} (mean = 333 kg hr^{-1}). This is expected as GAO has better detection sensitivity. The operational altitude of GAO was 4.5 km—resulting in less atmospheric interference and a smaller surface footprint—compared to the ANG's 8 km altitude (GAO $l_i = 4.5$ m footprint compared to ANG's $l_i = 8$ m footprint).

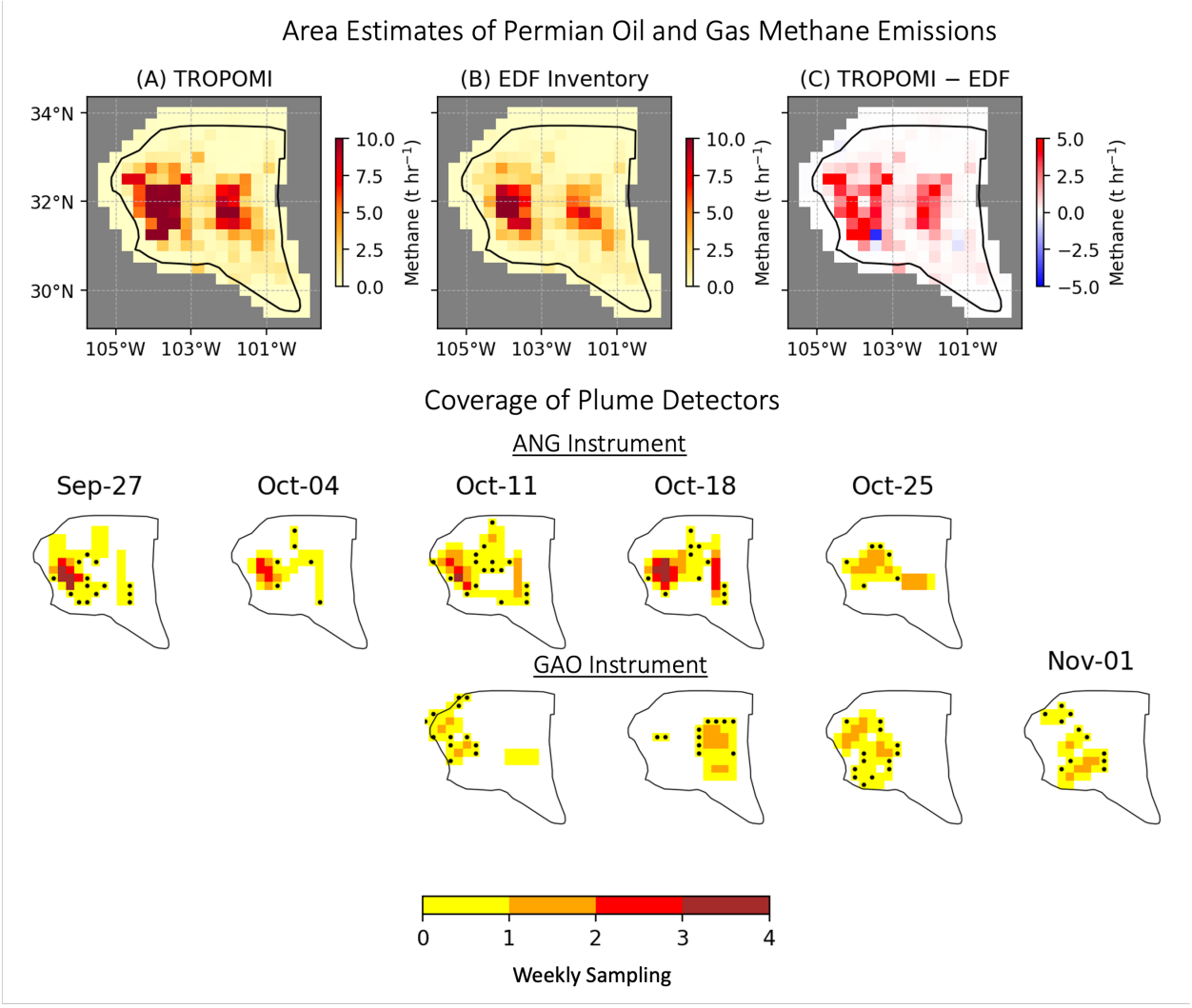

Figure 3: Permian emissions dataset used in this study. The top row shows the gridded area estimates from TROPOMI (top-down) flux inversion (A) and EDF (bottom-up) inventory (B) for the Permian Basin oil and gas emissions, with a spatial resolution of $0.25° \times 0.3125°$ latitude-longitude. The EDF inventory was prepared for the year 2018, while the TROPOMI estimates shown here are the six-week (September 24 to November 4, 2019) mean of the flux inversion posterior from Varon et al.[9]. The thick black contour marks the geological extent of the Permian Basin, highlighting two major hotspots of emissions corresponding to the Delaware (West) and Midland (East) basins. The middle and bottom rows show the weekly spatial coverage of plume detectors for the Fall 2019 Carbon Mapper survey in the Permian Basin. The sampling factor η for the ANG and GAO instruments is given for the weekly grid cells of 0.25×0.3125 degrees latitude-longitude. η exceeds 1 when a grid cell was observed more than once a week. Black dots indicate cells with a $\eta < 0.1$. Also see Table 1.

Moreover, GAO augmented its plume observations with high-resolution visual imagery to enhance detection accuracy and minimize surface artifacts (see Section B.2).

The Standard Deviation (SD) for ANG weekly PDFs expected values is 13% (relative to the multi-week mean of the weekly expected values). For GAO, the corresponding SD has a larger value of 28%. The ANG instrument's survey was strategically designed to repeatedly observe regions with high emissions (see Figure 3), whereas the GAO survey aimed to cover the entire Permian Basin at least once. Thus, GAO encountered a wider range of observation conditions than ANG, leading to a wider range of POD functions and the expected values of weekly detections.

Figure 4 also shows the High-Resolution Rapid Refresh (HRRR) model 10-meter wind speed data, which were used for emission rate quantification of the plumes by Cusworth et al.[68]. POD is sensitive to wind speeds[58]. The strong variation in observational conditions of GAO is reflected in the weekly wind speed distributions, with GAO's weekly wind speed expected values' SD at 45% compared to ANG's at only 20% (relative to the multi-week mean wind speeds). The larger variation in GAO's wind speeds results in greater variability in its POD and, consequently, in more diverse plume PDFs. For GAO, there is a noticeable and correlated distinction in emission rates PDF and wind distributions between two sets of weeks; the weeks of Oct-11 and Oct-18 differ significantly from Oct-25 and Nov-01. The R^2 between the weekly expected values of the log of wind speed and the log of emission rates is 0.98 for GAO and 0.44 for ANG, suggesting a strong influence of winds on the observed plume PDFs.

Despite the plume detections from different observation locations within the Permian Basin (Figure 3), the shape of the distributions for GAO and ANG are quite similar across the weeks, with major differences explained by wind speed variations and other spatial factors affecting the POD. After considering these variations, the PDF of the point source emission rates of the Permian Basin across this period can be assumed to be strongly correlated in time.

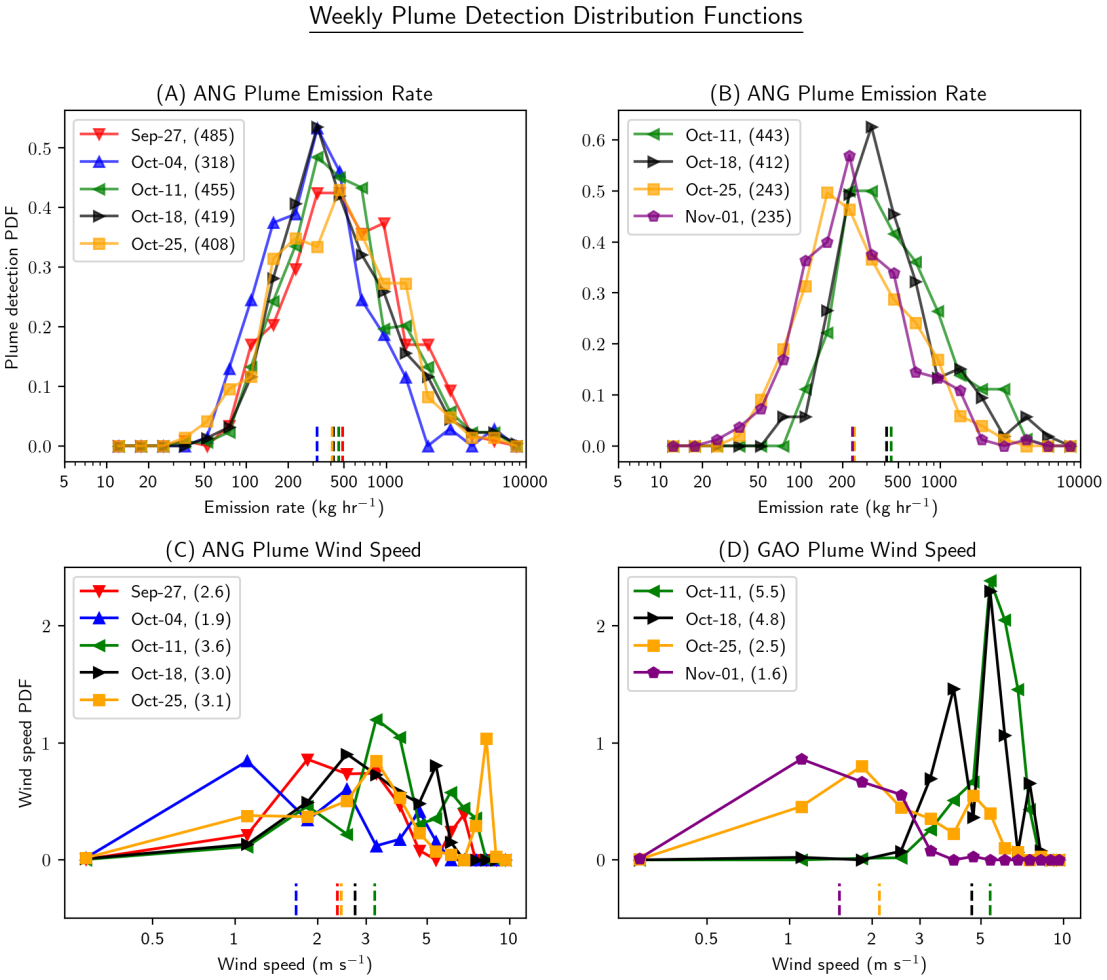

Figure 4: Probability Density Functions (PDFs) of methane plume detections by ANG and GAO aircraft instruments during the Fall 2019 Carbon Mapper survey in the Permian Basin. The top panels display the weekly emission rate PDFs. The bottom panels show the corresponding weekly wind speed PDFs. Each line color corresponds to a different week, as indicated in the legends. The emission rates and wind speeds are binned in logarithmic intervals. The expected values of the weekly distributions are given in the legends' parentheses and marked with the colored vertical lines at the bottom of each panel.

4.2 Comparison of Plume Emission Rate Sums with Area Estimates

We evaluate the relationship between plume emission rate sums and area estimates of the Permian Basin emissions. Figure 5 shows the time series of weekly plume sums and area estimates from the top-down TROPOMI and bottom-up 2018 EDF inventory, adjusted for aircraft sampling η. The correlation between the plumes and concurrent top-down area estimates is very strong, with GAO $R^2 = 1.0$ (P = 0.001) and ANG $R^2 = 0.95$ (P= 0.005). The 2018 EDF inventory has information on the spatial patterns of the emissions in the Permian, but it is constant across weeks, and it has no information from the six weeks of the fall of 2019. However, The temporal variability of the η adds variability to the product (ηx).

As expected, the correlations are lower: GAO $R^2 = 0.84$ (P= 0.09) and ANG $R^2 = 0.59$ (P = 0.13). These overall high correlation values show that Equation 1 is a good mathematical relation between area estimates and plume sums across large spatial domains like the Permian. The better correlation of independent plume sums with TROPOMI estimates than with temporally constant EDF estimates shows that TROPOMI's temporal variability is closer to the truth.

Figure 6.A presents the R^2 between area estimates and plume detection counts and emission rate means. The mean of plumes correlates negligibly with area estimates ($R^2 \leq$ 0.26 for both EDF and TROPOMI). For GAO, R^2 goes up to 0.26, but it has a large uncertainty, as indicated by a large P value (P = 0.51). A natural implication of a strong correlation with plume sums but no correlation with plume means is that there should be a correlation between the number of plume detections and area estimates. This hypothesis is also supported by the empirical tests (R^2 range of 0.31-0.78 for top-down).

Figure 6.B presents the R^2 at the grid cell level ($\eta_{ic} x_{cs}$ vs. y_{ics}). As anticipated, R^2 diminishes at smaller spatial scales due to increased noise. With plume means, R^2 is negligible for both bottom-up and top-down estimates. The plume sum R^2 values with the bottom-up EDF inventory are $R^2 = 0.63$ and 0.44 for ANG and GAO surpassing those with the top-

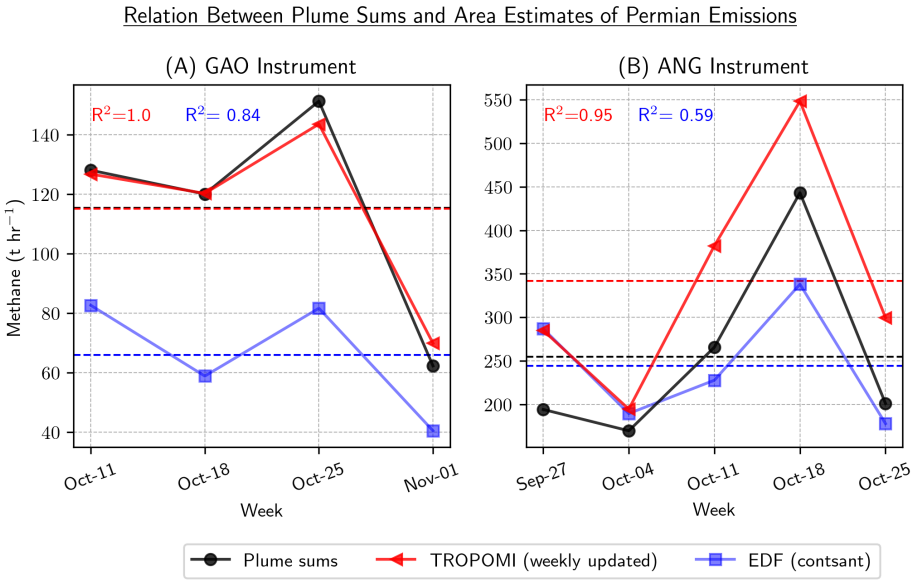

Figure 5: Comparison of time series of weekly plume emission sums ($= \sum_{c \in \text{Permian}} y_{ics}$) and area emission estimates. The top-down area estimates (concurrent weekly TROPOMI flux inversion) are shown in red, and bottom-up area estimates (annual 2018 EDF inventory) are shown in blue. The area estimates are adjusted for instruments' sampling ($= \sum_{c \in \text{Permian}} \eta_{ic} x_{cs}$). The R^2 of area estimates with plume sums are given in the respective colors. The dashed horizontal lines mark the means of the time series.

down TROPOMI, where the respective $R^2 = 0.58$ and $= 0.32$ for (P values for all grid scale plume sum $R^2 < 1^{-15}$). The better correlation of ANG with area emissions might be due to more extensive sampling of the emissions field by ANG under more consistent observation conditions than GAO.

The independence of errors in plume sums, EDF inventory, and TROPOMI estimates is expected when representing true emissions. In the quasi-Kalman-filter approach of Varon et al.[9], the posterior estimates are nearly independent of the EDF inventory prior used only for the first week of the multi-year inversion. Given the independence among the three estimates, an agreement between any two of these independent estimates, with poor agreement with the third, would suggest that the first two are closer to the truth. A poorer correlation of plume sums with TROPOMI flux inversions suggests that the EDF bottom-up inventory and plume data have superior spatial information at fine scales. This also indicates that TROPOMI is less effective at high spatial resolutions for constraining emissions, likely

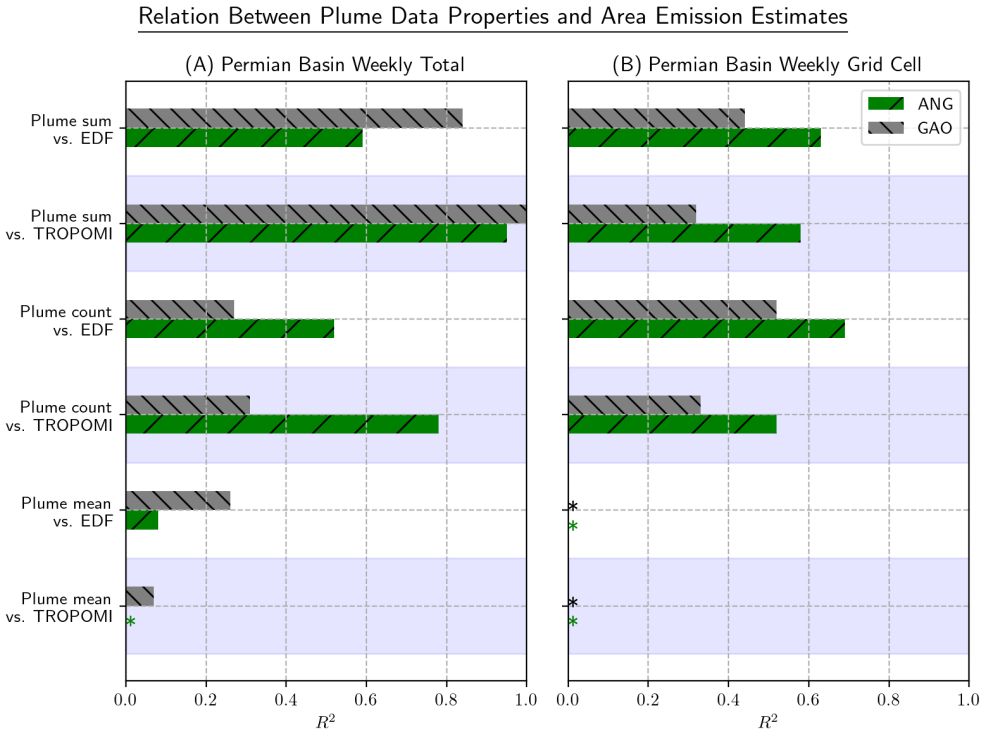

Figure 6: Correlation (R^2) between properties of weekly plume detections and sampling-adjusted area estimates. Panel (A) shows the correlation at the grid cell level ($\eta_{ic}x_{cs}$ vs. y_{ics}). Panel (B) shows the correlation for the Permian aggregate ($\sum_{c\in\text{Permian}} \eta_{ic}x_{cs}$ vs. $\sum_{c\in\text{Permian}} y_{ics}$). The plot compares the plume emission rate means, sums, and the number of plumes (count) with top-down (TROPOMI, light-blue shaded regions) and bottom-up (EDF) area estimates. Green bars represent ANG data, while gray bars represent GAO data. R^2 values of < 0.02 are marked with "*".

due to limitations in the CTM and TROPOMI coverage and resolution. The plume data show that the TROPOMI inversion's total weekly emission estimates for the Permian are better than EDF, but this might not be the case at fine spatial scales. Assimilating plume sums can be a promising approach to improve the fine-scale features in flux inversion estimates. This will be explored further in Section 5.2.

4.3 Correlation of Plume PDFs

Our empirical analysis shows that the mean of plume emission rates across space and time does not correlate with area estimates for a sector, whereas the sums of emission rates (and, to a lesser extent, the number of plume detections) exhibit a strong correlation. These

empirical observations can be explained by a hypothesis that true PDFs of point source emission rates within a sector are highly correlated in space and time, remaining nearly invariant over regional spatial and temporal intervals, such as the Permian Basin emissions over several weeks. In Figure 4, we showed that variations in the observed plume PDFs (function of point source PDF and instrument POD) and their expected values of observed plume detections are predominantly driven by changes in the POD of plume detectors due to fluctuations in wind speeds. As factors such as wind speed changes over a few weeks are expected to be uncorrelated with total methane emission variations, the expected values of observed plume PDFs are thus uncorrelated with area estimates.

The spatial and temporal correlation of point source PDFs can be physically explained as follows: The distribution of point source emissions of a sector is contingent upon (1) the proportions of different components (values vs. small pipes vs. large pipes vs. well heads, etc.,) and (2) the maintenance and quality of emission-causing components. These factors are correlated as they are shaped by technological, economic, and regulatory contexts, which exhibit spatial and temporal correlations. The point source PDF of a sector in a region is determined by the proportions of components and their respective emission PDFs. Thus, point source PDFs for sectors such as oil and gas within a unified administrative boundary, such as the Permian Basin, are expected to be similar. Plume PDFs are likewise correlated because they represent spatial aggregations of point source emission PDFs at the emission spatial resolution of the plume-detecting instruments (see Section 2.3). Different administrative and economic regions, such as oil and gas operations in Turkmenistan vs. the Permian Basin, can exhibit very different PDFs. For instance, Turkmenistan has a significantly higher number of large emitters exceeding 1000 kg hr^{-1} [70].

5 Applications

5.1 Evaluating Area Estimates Using Plume Detections

The previous section showed that plume detection sums exhibit strong correlations with area estimates. This enables the use of plumes to evaluate area estimates. The discrepancy between the correlation of plume sums with temporally variable top-down and constant bottom-up emissions provides insights into the ability of plume observations to evaluate temporal variations in emissions. We define a metric ϕ_T *plume temporal consistency* measure of a set of plumes.

$$\phi_T = R^2_{\mathrm{TS}} - R^2_{\mathrm{S}} \tag{4}$$

Here, R^2_{TS} is the correlation of plume sums with area estimate with both temporal and spatial variations, while R^2_{S} is constant in time and has only spatial variation. Subtracting the correlation with constant emissions removes the R^2 dependence of the spatial patterns of emissions and the sampling factor η .

We use the correlation of plume sums with EDF and TROPOMI as R^2_{TS} and R^2_{S}, respectively, to test the capability of the ANG and GAO plumes. The value of ϕ_T is 0.36 for ANG and 0.16 for GAO when considering all plumes (Figure 5 difference between the R^2 for TROPOMI and EDF). The modest ϕ_T for GAO is likely due to its lower sampling frequency (993 plumes over 4 weeks) of the emission field and the stronger variations in observation conditions. In contrast, ANG performed repeated observations in the emission-dense regions of the Permian Basin, leading to a detection count of 1954 plumes over 5 weeks, approximately double the number detected by GAO.

An important implication of our PDF correlation assertion (Section 4.3) is that plume instruments with detection sensitivities poorer than those of ANG and GAO should also be capable of predicting variations in area emissions. If the shape of the underlying full point source PDF remains stable, then the tail of the PDF observed by the instrument with poor sensitivity also constrains the total area emissions (Equation 6). Consequently, the sum of

the tail of the frequency distribution of detected plumes by any instrument should scale with area estimates.

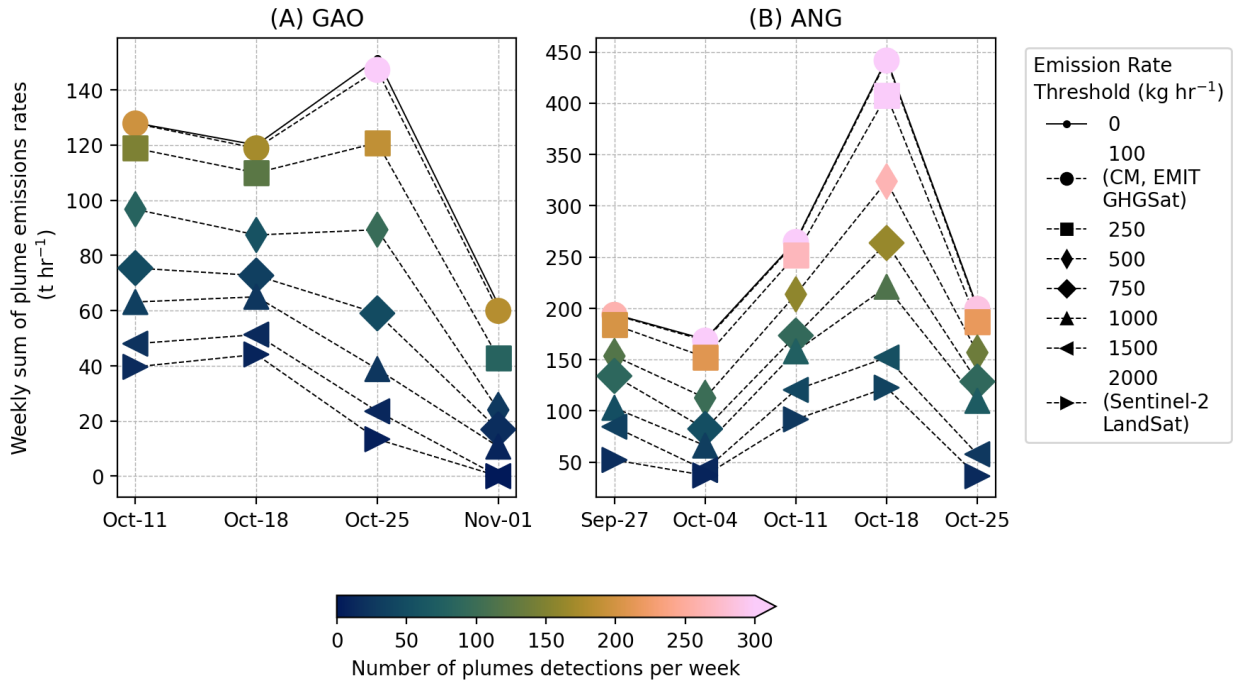

Figure 7: Weekly sum of Permian oil and gas plume detections for ANG and GAO instruments when plumes are filtered at different emission rate thresholds (plumes below the threshold are discarded). The figure shows that the temporal variability of the plume emission rate sums remains nearly unchanged across different emission rate thresholds. The legend gives an example of satellite plume instruments that are expected to have a detection limit range to be roughly around the threshold. The colors of the markers denote the number of plumes remaining each week after implementing the thresholds.

The 50 % POD (P_{50}) for the ANG and GAO instrument used in the Permian survey ranges from 50 to 300 kg hr^{-1} [30,57]. In comparison, most satellite instruments are expected to have poorer detection sensitivity with P_{50} around 1000 kg hr^{-1} (although their detection capability can identify plumes well below 100 kg hr^{-1} under favorable observation conditions). Figure 7 shows the temporal distribution of the plume sums from ANG and GAO after applying different emission rate thresholds, excluding detections below a threshold and including fewer plumes with high emission rates. The overall shape of the weekly sum time series remains similar, even when a threshold of 2000 kg hr^{-1} is applied, which is the sensitivity of Sentinel-2 and Landsat instruments. To test this hypothesis, we evaluated

R^2 correlations between TROPOMI and plume sums but only considered plumes above a certain detection threshold.

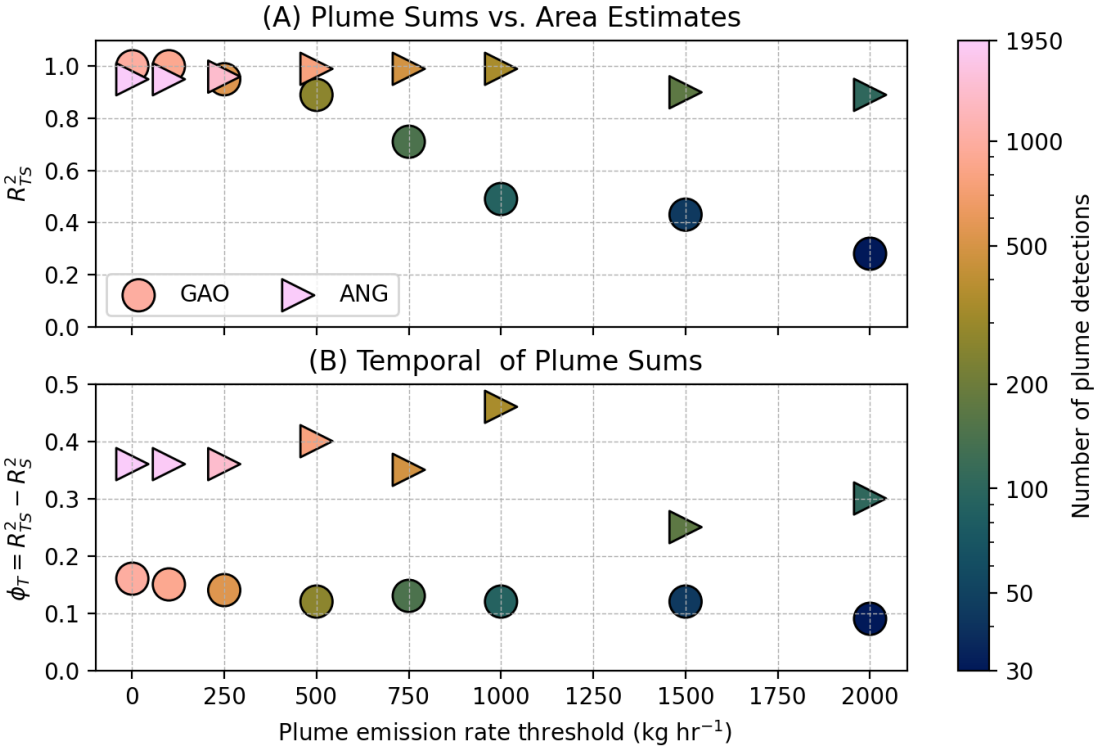

Figure 8: Relation between plume sums and area estimates of Permian oil and gas emissions as a function of plume emission rate threshold. Panel (A) shows the R^2 values for the sum of plume detections for the GAO (circles) and ANG (triangles) instruments related to top-down TROPOMI flux inversion estimates. Panel (B) shows the plume temporal consistency (ϕ_T) of plume sums as a function of the emission rate threshold. Both panels represent these metrics for plumes exceeding certain emission rate thresholds (x-axis), with colors denoting the number of plumes over the 6-week period. This setup illustrates that both R^2 and ϕ metrics remain stable across various thresholds.

Figure 8 shows the correlation between area and plume sums after applying emission rate thresholds. For the ANG instrument, starting with a zero threshold R^2_{TS} of 0.95 with 1954 plumes, R^2_{TS} remains stable at 0.88, even with large thresholds up to 2000 kg hr^{-1} with only 103 plumes. For the GAO instrument, $R^2_{\text{TS}} = 1$ at zero emission rate threshold, but shows a marked decline after 750 kg hr^{-1} threshold, with only 143 plumes remaining. Notably, an R^2_{TS} of 0.28 is maintained even with 29 GAO plumes at the 2000 kg hr^{-1} threshold. The sharp decrease in R^2_{TS} for GAO at high thresholds can be attributed to the low sampling

of GAO, resulting in fewer plume detections and the more diverse observational conditions encountered by GAO. Figure 8 also shows the temporal emission sensitivity metric ϕ. We find that ϕ is mostly independent of the emission rate thresholds. Surprisingly, ϕ of GAO remains stable across thresholds even though the R^2_{TS} values drop. The likely cause of this is that the errors added to the GAO plume sum time series with a lower number of plumes are uncorrelated with area emission variability. Therefore, the errors affect R^2_{TS} and R^2_{S} similarly, and the difference between the two remains unchanged. Overall, our analysis shows that satellite plume instruments, despite their lower detection sensitivity, can evaluate area emission estimates. Our findings align with Lauvaux et al. [71] and Ehret et al. [53], who proposed that detected plume emission rates follow a consistent global and regional patterns. Overall, we propose that plume detections can serve as proxies for unobserved smaller emissions in some sectors, enabling the estimation and/or evaluation of total area emissions.

5.2 Bayesian Plume Inversion

Current atmospheric flux inversion methods use satellite or in situ concentration observations and a CTM to inform grid-scale area estimates. Plume detections offer independent emission observations and can improve area estimates. We derived and tested a statistical relationship between plume emission rate sums and area estimates. Using the plume sum model (Equation 1), we perform Bayesian assimilation of gridded plume sums (referred to as *plume inversion*) to inform grid cell area estimates.

5.2.1 Plume Inversion Setup

Our plume inversions optimize a state vector representing weekly area estimates (from Tuesday to Monday) from September 24 to November 4, 2019, at a 25 $\times$ 25 km^2 resolution grid within the Permian for the oil and gas sector. Per week, 235 state vector elements are optimized. We call these plume inversions Plume-EDF and Plume-TRO. We refer to the priors used in these inversions as EDF and TROPOMI estimates. We refer to the max-

imum a posteriori (MAP) solutions for these inversions as Plume-EDF and Plume-TRO, respectively. As per Equation 1, the weekly plume factor and temporal sampling bias need to be determined to relate area estimates and plume sums. Table 1 presents the weekly values of $\tau\kappa$ and η. The mean (and uncertainty) of the weekly $\tau\kappa$ are derived by comparing TROPOMI and plume data. Because $\tau\kappa$ are properties of the instrument and emission sectors, the TROPOMI-derived $\tau\kappa$ values are used for Plume-EDF and Plume-TRO inversions. Our plume inversion methodology is detailed in Appendix Section A.2.

5.2.2 Weekly Total Permian Emissions

Figure 9 shows the total weekly emission estimates from the plume inversions. Degrees of Freedom for Signal (DOFS) values in the figure represent the magnitude of observational constraint provided by the plumes in the inversion (Equation 15). For both inversions, the weeks with large DOFS (Oct-11, Oct-18, Oct-25) coincide with the periods when both GAO and ANG instruments are surveying (see Figure 3). During these weeks, the DOFS range for the two instruments is 28–38. In the other three weeks, when only one instrument is surveying, the DOFS range is 11–20.

The Plume-TRO inversion's adjustment to the TROPOMI prior is minor overall, resulting in an increase of 3% over a 6-week mean (from 462 ± 8.24 to 472 ± 6.55 t hr^{-1}). This outcome is expected, given that TROPOMI prior emissions serve to anchor the plume constraint, with $\tau\kappa$ quantified from TROPOMI estimates (see Equation 3). On a weekly basis, a substantial 13% adjustment is noted for the week of Oct-11 (from 455 ± 23.3 to 513 ± 17.6 t hr^{-1}) in Plume-TRO inversion. Other weeks exhibit smaller adjustments, ranging from -5% to $+6\%$. During the week of Oct-11, the flux inversion by Varon et al.[9] had the lowest DOFS (2.2 for a state vector with 235 elements), indicating insufficient constraint on the emissions by TROPOMI data. In contrast, other weeks displayed higher DOFS values in Varon et al.[9] inversion (2.3–8.3). The fact that the most significant adjustments in Plume-TRO inversions occur when TROPOMI estimates are most uncertain suggests that plume

observations improve the area emission estimates' accuracy.

Strong adjustments are observed in the Plume-EDF inversion, with plume assimilation increasing the 6-week mean by 30% (from 294 ± 16 to 380 ± 9 t hr^{-1}). This adjustment brings the posterior, Plume-EDF, into better agreement with TROPOMI estimates, reducing the initial 36% underestimation to 18%. Across the weeks, plumes adjust emissions towards TROPOMI (and Plume-TRO) estimates, particularly during weeks with high DOFS. Notably, for the week of Oct-11, the Plume-EDF (456 ± 20 t hr^{-1}) and TROPOMI estimates (454 ± 23 t hr^{-1}) are very close, highlighting the impact of plume data constraint. For the week of Sep-27, TROPOMI estimates align with the EDF, and the DOFS is minimal, resulting in minimal adjustment by Plume-EDF inversion. Conversely, during the week of November 1st, despite much larger TROPOMI estimates, the low Plume-EDF inversion's DOFS (17) leads to an insignificant adjustment of the EDF estimates. Excluding the week of Nov-1, the plume inversion improves the R^2 from 0 (constant EDF estimates) to 0.79 (P = 0.04). Our analysis shows that plume data can improve the accuracy of regional total area emission estimates.

5.2.3 Spatial Patterns

Figure 10 shows the mean grid-scale emissions for the Plume-EDF and Plume-TRO inversions. The Plume-EDF inversion increases the emissions in most of the grid cells, and the magnitude of emissions becomes similar to the TROPOMI estimates. Both inversions have DOFS hot spots following the spatial pattern of the two major oil and gas production regions: the Delaware (West) and Midland (East) Basins. This is expected, as the plume surveys targeted these major oil and gas production regions. The plume inversion also improves (reduces) the cross-correlation among area emission grid cells. (See Figure 11). Flux inversions assimilating concentration data induce cross-correlations between grid cells across spatial, temporal, and sectoral domains due to the limitations in resolving the sensitivities across multiple grid cells, often constrained by limited observational data or the resolution of

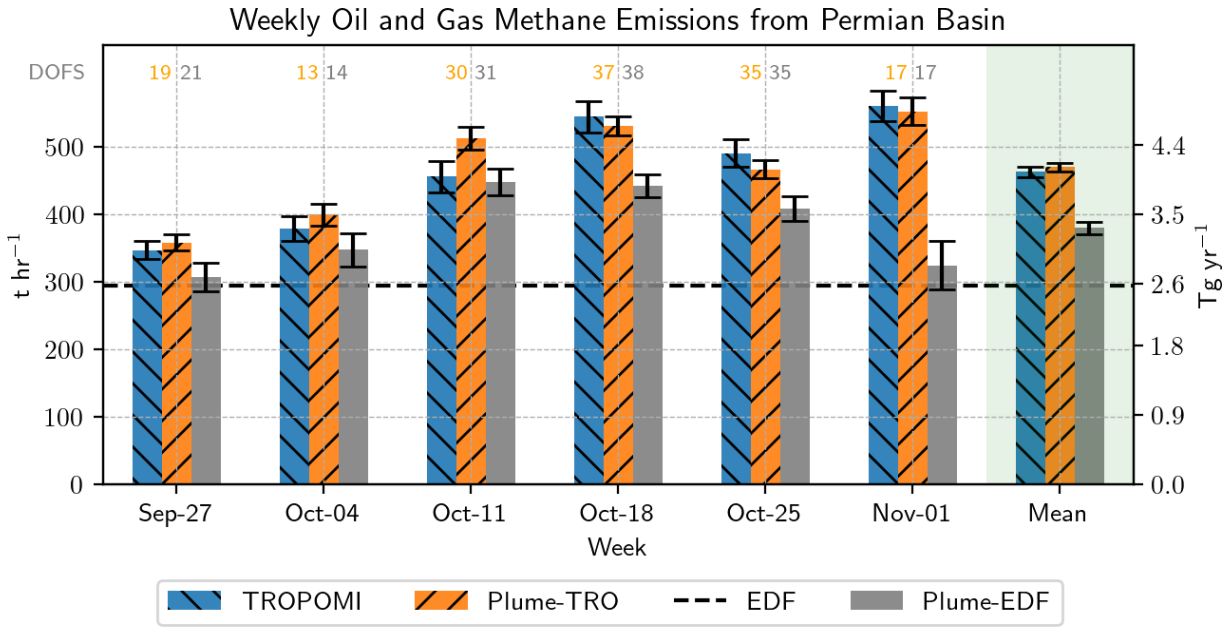

Figure 9: Weekly methane emission estimates for the Permian oil and gas sector. The dashed horizontal line represents the EDF inventory. 'TROPOMI' and 'Plume-TRO' denote the prior and posterior for the plume inversion performed on TROPOMI emission estimates, respectively. Similarly, 'EDF' and 'Plume-EDF' represent the prior and posterior for the EDF plume inversion. The DOFS values (orange for Plume-TRO inversion and gray for Plume-EDF inversion) above each bar indicate the level of observational constraint in the inversions. The right-most group of bars gives the mean values across the weeks. Error bars indicate one standard deviation uncertainty.

CTM. Given plumes' near-perfect spatial and sectoral attribution, their assimilation reduces the off-diagonal elements of the correlation matrix, enhancing the spatial specificity of the area emission estimates.

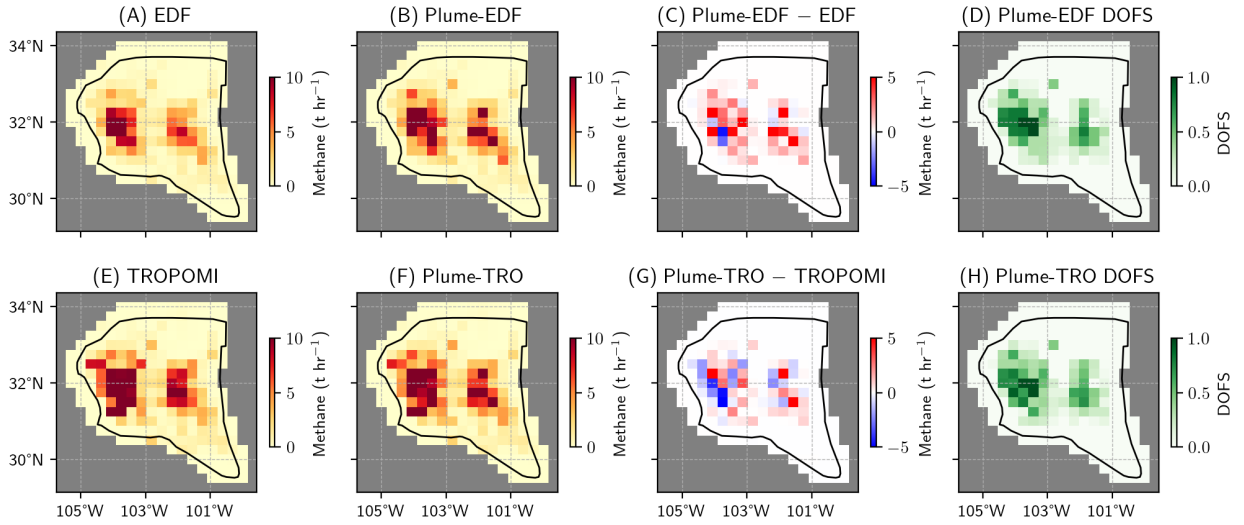

Figure 10: Six-week mean grid-scale emission maps from plume inversions. Panels (A) and (E) show the EDF and TROPOMI plume inversions' priors, respectively. Panels (B) and (F) display the posterior emissions of plume inversions, while Panels (C) and (G) show the updates from the plume inversions. Panels (D) and (H) present the Degrees of Freedom (DOFS) per pixel, indicating the observational constraints over the six-week period.

6 Discussion

6.1 Plume Constraint on Area Emissions Estimates

The plume data record is expanding rapidly, with plumes now regularly observed by numerous aircraft and satellite instruments[72]. We have presented a method to utilize plume detections to evaluate and inform total regional emission estimates. Our approach benefits flux inversion and bottom-up modelers in several ways. First, our approach represents a no-cost gain on the existing area estimation infrastructure. Plume detections, primarily employed for Leak Detection and Repair (LDAR) methods, thus become a cost-effective option for providing additional top-down constraints on area estimates. Conversely, data from non-

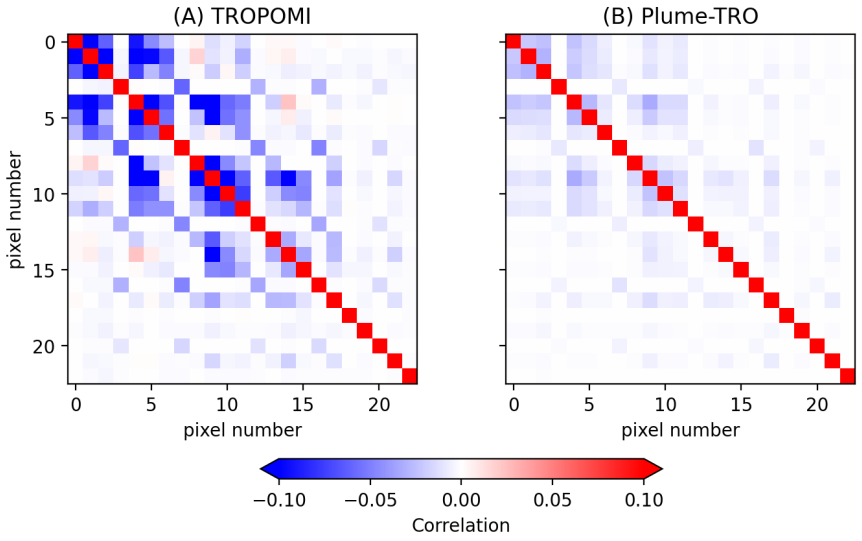

Figure 11: Improvement of the error correlation matrix by the Plume-TRO inversion for the week of Sep-27. Panel (A) shows the prior, and Panel (B) shows the posterior error correlation matrices of the Plume-TRO inversion. Only grid cells with plume detections during the week are shown.

imaging concentration satellites like the Greenhouse gases Observing SATellite (GOSAT) are mostly used for flux inversions. Second, plume detections provide fine spatial, temporal, and sectoral specificity, a feat particularly challenging for conventional top-down methods, which rely on limited-resolution numerical approximation of chaotic atmospheric transport. Third, plume detections provide information on the emission processes, especially in identifying anomalous emissions and their contributions to total emissions, which can lead to the improvement of bottom-up models[8,38].

Our study has focused on plume detection from imaging instruments onboard aircraft and satellites. Many surveys use on-ground or aerial in-situ instruments to estimate component or facility-scale emissions[1,73–75]. These emission datasets have very similar properties to the aircraft and satellite plume datasets from imaging instruments as they provide location, time, and emission rate estimates. The gridded sum of such in-situ-based plume datasets can also be used to evaluate area estimates or in a plume inversion.

6.2 Co-assimilation of Plume and Concentration data

Our plume inversion method provides an approach for using fine-spatial-scale plume information from concentration imaging instruments to constrain area emissions. Almost all methane-concentration-imaging area mappers observe methane plumes[54]. For example, TROPOMI methane plumes have been detected from single point sources[56,71] and clusters of point sources[51].

Using our plume inversion approach, the co-assimilation of plume and area information is particularly relevant for new and upcoming imaging satellites that will provide concentration constraints and detect plumes with small spatial footprints. The recently launched MethaneSAT satellite instrument has a footprint size of 100 meters by 400 meters and a 200-kilometer swath[76]. The proposed Carbon-I NASA Earth System Explorer mission will observe at a 400-meter spatial footprint in normal (non-target) operation mode[77]. These instruments will detect methane plumes and provide top-down concentration constraints for flux inversions. Suppose a CTM with 25 $\times$ 25 km^2 spatial resolution is used in an inversion assimilating the 400-meter footprint observations. In that case, the inversion cannot use any concentration gradient information finer than 25 $\times$ 25 km^2. The plume inversion approach can maximize the use of information from these satellite observations to inform area emission estimates.

6.3 Periodicity of Permian oil and gas emissions

Some studies have investigated the extent to which area estimates can be accounted for by plume detections[30,43,59,60,68], while others have attempted to estimate country-scale emissions using point sources within the oil and gas sector in the USA[6,8,44] and across basins[37,38]. These studies utilize plume detections to refine emission factors and employ a bottom-up extrapolation approach assuming persistence characteristics. However, the temporal bias of plume detection emissions is not always accounted for, which can potentially result in the overestimation of emissions. Oil and gas production emissions have been shown to exhibit significant

periodicity due to activities such as manual liquid unloading and maintenance operations, which typically occur during afternoon working hours[59,74]. Consequently, instruments that favor afternoon observations are likely to exhibit overestimation.

Our analysis indicates a diurnal periodicity in the Permian Basin oil and gas emissions, indicated by the high values for the product of plume factors and temporal bias (weekly $\tau\kappa$ range 0.89–1.05 for GAO instruments). Theoretically, $\tau \leq 1$. We expect true τ to be around 0.5 for the AVIRIS-NG (a combination of GAO and ANG) in the Permian Basin, considering Kunkel et al.[30] showed that many small plumes are not detected by AVIRIS-NG. The observed $\tau\kappa$ can only be explained by $\kappa > 1$. Even though TROPOMI also observes during the afternoon, region-scale TROPOMI inversion estimates are expected to have a smaller temporal bias since they are sensitive to emission history from the past hours/days. It is possible that our $\tau\kappa$ estimates may be high due to the underestimation of Permian emissions by TROPOMI inversion.

We advocate for future studies to consider emission periodicity when calculating mean emissions using afternoon or daytime observing instruments. The periodicity bias can be assessed using bottom-up information. An optimal plume survey strategy could be devised to measure the periodicity of a sector's emissions. For instance, continuous observation of a small area in the Permian Basin for a full day, including nighttime detections using aerial LIDAR instruments or grounded in situ instruments, could help quantify the diurnal cycle of emissions.

6.4 Comparison of Plumes from Different Instruments

Our work has implications for comparing plume emission rates from instruments with different spatial footprints, especially in dense point source emission fields like oil and gas basins. We showed that coarser footprint instruments can capture emissions from more point sources than finer footprint instruments, making direct comparisons difficult without accounting for contributions from small point sources (Figure 1). We illustrated the effect of footprint

size resolution on the observed distribution of plume emission rates (Figure 2). Kunkel et al.[30] estimated the POD curve for the AVIRIS-NG instrument using LIDAR plume detections, noting that differing spatial resolutions could introduce biases. They aggregated LIDAR detections to a facility scale to match AVIRIS-NG's resolution, mitigating some biases. However, our theory suggests that AVIRIS-NG plumes may still show higher emission rates due to small sources undetected by LIDAR, potentially overestimating the POD for AVIRIS-NG. The aggregation effect depends on the distribution of point sources and plume area used for emission rate quantification.

The plume aggregation effect is relevant for comparing emission rates of trace gases like CO_2 and NO_2[78,79]. For instance, CO_2 plumes observed by coarse-resolution satellites (e.g., OCO-3) cover larger areas and show higher emission rates than those observed by fine-resolution satellites (e.g., PRISMA, EnMAP, EMIT) that observe plumes from specific sources like a power plant's smokestack[78,80].

7 Summary

We presented theoretical and empirical analyses to relate emission rate sums of sporadic plume detections with area estimates in dense point source emission fields. We used oil and gas sector emission data from the Permian Basin to show a strong linear relationship between plume sums and area estimates. This relationship enables the use of plume detections to evaluate and inform area estimates. After accounting for the plume detectors' sampling of the Permian emission field, we found that the weekly plume sums demonstrate a strong correlation with TROPOMI flux inversion area estimates. We demonstrated that the correlation remains robust, even with as few as 100 large plumes over a period of four to five weeks. This demonstration implies that informing area estimates should also be possible using space-borne plume detectors, which have poorer detection sensitivity than aircraft instruments but have a significant advantage in spatial and temporal coverage. We presented

a Bayesian framework to inform gridded area estimates using plume data. We improved the posterior's temporal variability by assimilating weekly plume sums on a temporally constant EDF inventory. By assimilating plume data, we corrected fine spatial resolution features of TROPOMI flux inversion emission estimates.

Plume detections are direct observations of emissions, enabling identification of the source location, sector, and time of large emissions. Area estimates constrain the total emissions, i.e., the area integral of the emission field. Both plume and area observation approaches provide unique and important information on emissions. Future research should expand the approach developed in this study to include a broader spectrum of methane source sectors and possibly other trace gases (CO_2, CO, NO_2) observed at different spatial scales as plumes and area emission estimates.

Acknowledgement

Part of this work was carried out at the Jet Propulsion Laboratory, California Institute of Technology, under a contract with the National Aeronautics and Space Administration (80NM0018D0004). This research is supported by NASA ROSES Grant 18-CMS18-0018, 22-CMS22-0010, and the U.S. Greenhouse Gas Center.

Competing Interests: The authors declare that they have no conflict of interest.

A Appendix

A.1 Derivation of Relation between Area Estimates and Plume Sums

We derive a statistical relation between the area estimates of grid cell emissions (representing mean emissions over a space and time interval) and the emission rate sum of plume detections from the grid cell. Consider a sector or sub-sector emission category s composed of densely distributed point sources within a large grid cell c of area l_c^2 [distance^2]. The size of l_c^2 ranges from 25×25 km^2 (a regional flux inversion grid cell) to more than $5^\circ \times 5^\circ$ of latitude–longitude (a global flux inversion grid cell).

Suppose a plume instrument i with a spatial footprint size of l_i observes c. The instrument performs v number of scans covering different portions within the period of c. From these scans, plume detections are identified and quantified. Let η_{ic} [unitless] represent the instrument's *sampling* of c, which is the ratio of the total scanned ground area to the grid cell area l_c^2. For example, if an instrument scans half of a grid cell once, $\eta_{ic} = 0.5$, and if it scans the entire grid cell once, $\eta_{ic} = 1$. Assuming a uniform or ergodic point source emission field, the number of plume detections in the second scenario would be twice that of the first scenario, shifting the entire frequency distribution up by a factor of two.

Suppose the emission spatial resolution of the instrument is δ_i. δ_i^2 is roughly average of the plume area sizes that the instrument observes. This means the instrument would effectively observe the emission field of c divided into $m = \left(\frac{l_c}{\delta_i}\right)^2$ small areas. Each δ_i^2-sized area will have an emission value e [mass time^{-1}].

Let $p_{ics}(e, \delta_i)$ represent the probability density function (PDF) of the pixels' emission values for pixels with $e > 0$, capturing the full emission distribution of point sources in sector s within cell c at resolution δ_i. The total emission (or area estimate) in c, denoted as

x_{cs} [mass time^{-1}], is given by:

$$x_{cs} = \alpha_{cs} m_{ic} \sum_{e} p_{cs}(e, \delta_i) e \tag{5}$$

Here, α_{cs} [unitless] is the emission activity factor in grid cell c. For example, α_{cs} could represent the number of gas wells in c when considering emissions from gas production. Notice that $\sum_e p_{cs}(e, l_i)e$ is the expected value corresponding to the PDF. The emission rate distribution shifts to the right as l_i (and δ_i) increases (see Figure 2). The expected value of the distribution shifts proportional to δ_i^2, so the quantity $m_{ic} \sum_e p_{cs}(e, l_i)e$ remains independent of δ_i. This is necessary because the total area estimate x_{cs} should not depend on the plume detecting instrument's properties.

Let $q_{ic}(e)$ denote the POD function of instrument i in the observation conditions of c. The frequency distribution ($f_{ics}(e)$) of observed plume emission rates can be modeled as:

$$f_{ics}(e) = \alpha_{cs} \eta_{ic} \kappa_{is} m_{ic} p_{cs}(e, \delta_i) q_{ic}(e) \tag{6}$$

Here, κ_{is} [unitless] is a periodicity correction factor to account for the temporal sampling bias of i observing plumes from s. If there is a difference between the observed sum of emissions and the temporal mean, then $\kappa_{is} \neq 1$. In a sector, there can be periodic, episodic, and continuous emissions. If l_c is sufficiently large to provide a representative sampling of independent and identically distributed (IID) episodic emitters, the contribution from episodic emissions can be considered constant in time due to ergodicity. Consequently, only the periodicity of the emissions causes a temporal sampling bias.

Let y_{ics} [mass time^{-1}] denote the sum of emission rates of the observed plumes by i in the v scans. Then,

$$y_{ics} = \alpha_{cs} \eta_{ic} \kappa_{is} m_{ic} \sum_{e} p_{cs}(e, \delta_i) q_{ic}(e) e \tag{7}$$

The relationship between the plume sum, y_{ics}, and the total area estimates x_{cs} can be

derived using Equations 7 and 5:

$$y_{ics} = \tau_{ics}\kappa_{is}\eta_{ic}x_{cs} \tag{8}$$

Here, the unitless quantity

$$\tau_{ics} = \frac{\sum_e p_{cs}(e, \delta_i)q_{ic}(e)e}{\sum_e p_{cs}(e, \delta_i)e} \in [0, 1] \tag{9}$$

represents the fraction of the total emissions of s that can be observed by i. If $\eta_{ic} = 1$ (one complete scan of c by i) and there is no periodicity bias ($\kappa_{is} = 1$), $\tau_{ics} = \frac{y_{ics}}{x_{cs}}$. We call τ the *plume factor*.

A.2 Bayesian Assimilation of Plume Observations

The information from plume detections and area estimates can be combined using Bayes' theorem. Let $\mathbf{x}$ be the area estimates vector, where an element of $\mathbf{x}$ represents the total area emissions from the grid cell. Let $\mathbf{y}$ be the plume sum observation vector, with elements representing the sum of emission rates of plume detections over the spatial and temporal intervals of the grid cell.

The conditional PDF $p(\mathbf{x}|\mathbf{y})$ of the area emission estimates vector $\mathbf{x}$ given the plume observation vector $\mathbf{y}$ is given by

$$p(\mathbf{x}|\mathbf{y}) = \frac{p(\mathbf{y}|\mathbf{x})p(\mathbf{x})}{p(\mathbf{y})} \tag{10}$$

Here, $p(\mathbf{y}|\mathbf{x})$ is the conditional PDF of the observed gridded plume sums given the area estimates. The functions $p(\mathbf{x})$ and $p(\mathbf{y})$ are prior PDF of $\mathbf{x}$ and $\mathbf{y}$, respectively. $\mathbf{x}$ and $\mathbf{y}$ have the following relation:

$$\mathbf{y} = \mathbf{K}\mathbf{x} + \epsilon, \tag{11}$$

where $\mathbf{K} = \frac{\partial \mathbf{y}}{\partial \mathbf{x}}$ is a Jacobian matrix, whose entries can be estimated via the plume sum

model (Equation 1). ϵ represents the combined errors in the observations and model. If the PDFs of $\mathbf{x}$ and $\mathbf{y}$ are assumed Gaussian, a quadratic cost function $J(\mathbf{x})$ can be derived as

$$-2\log p(\mathbf{y}|\mathbf{x}) \sim J(\mathbf{x}) = \underbrace{(\mathbf{x}-\mathbf{x_A})^T\mathbf{S_A}^{-1}(\mathbf{x}-\mathbf{x_A})}_{\text{Prior Constraint}} + \underbrace{(\mathbf{y}-\mathbf{Kx})^T\mathbf{S_\epsilon}^{-1}(\mathbf{y}-\mathbf{Kx})}_{\text{Observation Constraint}} \tag{12}$$

Here, $\mathbf{x_A}$ is a prior estimate of the area estimates vector, and $\mathbf{S_A}$ and $\mathbf{S_\epsilon}$ represent the prior and observational error covariance matrices on $\mathbf{x}$ and ϵ, respectively. The derivation of the cost function is provided in Lorenc[81], Brasseur and Jacob[82]. The cost function comprises two components: the error-weighted prior constraint and the error-weighted observational constraint. The minimization of the cost function yields the maximum a posteriori (MAP) solution, represented as the posterior area estimate vector $\hat{\mathbf{x}}$:

$$\hat{\mathbf{x}} = \mathbf{x_A} + \hat{\mathbf{S}}\mathbf{K}^T\mathbf{S_\epsilon}^{-1}(\mathbf{y}-\mathbf{Kx_A}) \tag{13}$$

Here, $\hat{\mathbf{S}}$ denotes the posterior error covariance matrix, given by:

$$\hat{\mathbf{S}} = (\mathbf{K}^T\mathbf{S_\epsilon}^{-1}\mathbf{K} + \mathbf{S_A}^{-1})^{-1} \tag{14}$$

The averaging kernel matrix, $\mathbf{A}$, quantifies the sensitivity of the posterior solution to the truth. It can be calculated as follows:

$$\mathbf{A} = \mathbf{I} - \hat{\mathbf{S}}\mathbf{S_A}^{-1} \tag{15}$$

Here, $\mathbf{I}$ is an identity matrix. The trace of matrix $\mathbf{A}$ (the sum of its diagonal elements) is the *degrees of freedom for signal* (DOFS) of the inversion. The DOFS indicates the number of pieces of information constraining the state vector in the inversion.

We performed plume inversion on the Permian Basin oil and gas emissions using ANG and GAO plume observations from the Fall 2019 Carbon Mapper campaigns. The state vector

$\mathbf{x}$ represents weekly area estimates (for the week period Tuesday to Monday) over six weeks (September 24 to November 4, 2019) for each grid cell of 25×25 km^2 ($0.25^\circ \times 0.3125^\circ$). Two plume inversion analyses were conducted using different priors: (1) constant bottom-up EDF inventory[69], and (2) The TROPOMI flux inversion from Varon et al.[9]. The posterior from the TROPOMI inversion performed by Varon et al.[9] is utilized as the prior for our plume inversion. TROPOMI area estimates give the total emission from all the sectors. Emissions sectors other than oil and gas contribute only 6 percent to the total emissions in the Permian. In conducting the TROPOMI inversion, these other emissions were estimated using the EDF inventory proportions and subtracted from the TROPOMI emission estimates.

$\mathbf{S_A}$ for the TROPOMI plume inversion is the posterior error covariance matrix of TROPOMI inversion from Varon et al.[9]. For the Plume-EDF inversion, $\mathbf{S_A}$ is assumed to be a diagonal matrix with 100 % standard deviation uncertainty.

The observation vector $\mathbf{y}$ is formed as:

$$\mathbf{y} = \begin{bmatrix} y_{i,1} & y_{i,2} & y_{i,3} & \cdots \end{bmatrix}^T, \text{ where } i \in \{\text{GAO}, \text{ANG}\} \tag{16}$$

Here, $y_{i,c}$ represents the sum of plume emission rates observed in the c-th grid cell (25×25 km^2) during a week period (Tuesday to Monday) by the instrument indexed by i. As per our model in Equation 1, the entries of the matrix $\mathbf{K}$ take the form:

$$k_{mn} = \begin{cases} \tau_{is}\kappa_{is}\eta_{ic} & \text{if } m = n = c \\ 0 & \text{otherwise} \end{cases} \tag{17}$$

where k_{mn} represents the element at the m-th row and n-th column of $\mathbf{K}$.

Table 1 presents the weekly $\tau_{is}\kappa_{is}$ and η_{ic} for the two instruments. For each instrument, we compute the mean of the weekly $\tau_{is}\kappa_{is}$ values. The uncertainty $\sigma_{\tau_{is}\kappa_{is}}$ is estimated as the 1 standard deviation ($\pm$) across the weekly values. We find $\tau_{is}\kappa_{is}$ values of 0.99 ± 0.06 for GAO and 0.75 ± 0.08 for ANG, respectively.

We modeled the observation error covariance matrix $\mathbf{S}_\epsilon$ as a diagonal matrix. All off-diagonal elements of $\mathbf{S}_\epsilon$ are set to zero. The diagonal elements at row and column m are calculated as the quadrature sum of plume observation error (σ_{y_m}), plume sum model error (σ_{k_m}), and sampling variance errors ($\sigma_{sampling_m}$).

$$\sigma^2_{\epsilon_m} = \sigma^2_{y_m} + \sigma^2_{sampling_m} + \sigma^2_{k_m} \tag{18}$$

where,

$$\sigma^2_{k_m} = \left(\frac{\sigma^2_{\tau_m \kappa_m}}{\tau^2_m \kappa^2_m} + \frac{\sigma^2_{\eta_m}}{\eta^2_m} \right) (\tau_m \kappa_m \eta_m x_{A_m})^2 \tag{19}$$

Here, x_{A_m} is the m^{th} element of $\mathbf{x_A}$. η_{ic} is calculated directly from the precise ground area of the flight tracks. The associated errors ($\sigma^2_{\eta_m}$) are negligible compared to other terms and are therefore disregarded in our plume inversions ($\sigma_{\eta_m} = 0$). $\sigma^2_{y_m}$ is calculated by adding the emission rate errors from the Carbon Mapper plume dataset in quadrature. $\sigma_{sampling_m}$ depends mainly on η_{ic}, decreasing with larger values of η_{ic}. We calculate it using the following relation:

$$\sigma_{sampling_m} = \frac{0.1}{\sqrt{\eta_m}} \tag{20}$$

This error model ensures that the sampling error diminishes with increased sampling, following the law of large numbers. A value of 0.1 t hr^{-1} is the assumed sampling error for one single complete scan of a grid cell.

B Data

B.1 Area Estimates of Emissions

EDF Bottom-up Inventory: We utilize the Environmental Defense Fund's (EDF) inventory as presented in Zhang et al.[69]. This inventory extrapolates methane emissions from ground-based measurements at several oil and gas production sites within the Permian Basin, focusing predominantly on the New Mexico area during July and August of 2018. The sites were categorized based on their complexity: simple sites (equipped with wellheads and/or pump jacks) and complex sites (additionally featuring storage tanks and/or compressors). By extending these individual site emission rates to encompass the entire Permian Basin, the inventory estimates a basin-level methane emission rate of 2.3 Tg year^{-1} from oil and gas production activities. The inventory further includes emissions from compressor stations and processing plants, estimated at 0.22 and 0.14 Tg year^{-1}, respectively. The EDF inventory subsequently disaggregates these emissions down to a 0.1° × 0.1° grid, aligning with the spatial distribution of gas production. An updated version of the EDF inventory was published in Omara et al.[75]. We still use the Zhang et al.[69] version in this study to maintain consistency with Varon et al.[9], who use this inventory as their Kalman Filter flux inversion prior.

TROPOMI Flux Inversion: We utilized the top-down methane emission data from the TROPOMI inversion analysis by Varon et al.[9]. They optimized emissions for the Permian basin at resolutions of 0.25° x 0.3125°, equating to about 25 × 25 km^2 in the Permian basin. The inversions used methane concentration observations from the TROPOspheric Monitoring Instrument (TROPOMI) on the Sentinel-5 Precursor satellite to estimate weekly methane emissions across the Permian Basin. TROPOMI, operational since May 2018, has a nadir-viewing push-broom configuration that effectively captures methane concentration observations with a swath of 2600 km. The inversion leveraged a nested version of the offline GEOS-Chem chemical transport model powered by NASA GEOS-FP meteorological fields.

The model is equipped with high-resolution grids and dynamic boundary conditions. The inversion utilized prior emission estimates from the 2018 EDF inventory discussed above. The GEOS-Chem chemical transport model acted as a forward model, relating emissions with the TROPOMI observations in a Bayesian inverse modeling framework. This framework aimed to minimize discrepancies between model predictions and observed data, constrained by prior emission estimates and error covariance matrices. The prior emissions were updated weekly, nudging closer to the original EDF bottom-up inventory values, thereby setting initial conditions for subsequent analyses. For detailed information on these methodologies and the inversion results, the reader is referred to Varon et al.[9]. The mean emissions for the 127 weeks (May 2018 to October 2020) were estimated to 4.05Tg yr^{-1}, 57% larger than the EDF 2018 inventory estimate of 2.58Tg yr^{-1}. Note that the weeks defined in Varon et al.[9] are from Tuesday to Monday of the next week, and we have used the same week period in our analysis.

B.2 Plume Observations

We use the plume detection data presented in Cusworth et al.[68]. The airborne survey, conducted by Carbon Mapper, aimed to quantify strong methane point sources in the Permian Basin. Between September and November 2019, Carbon Mapper deployed two remote sensing airborne platforms to map the region: the Next-Generation Airborne Visible/Infrared Imaging Spectrometer (AVIRIS-NG, henceforth referred to as ANG) and the Global Airborne Observatory (GAO). The GAO imaging spectrometer is identical to the ANG instrument; the NASA Jet Propulsion Laboratory constructed both around the same time. GAO is equipped with a Digital Modular Aerial Camera (DIMAC), bore-sighted with the imaging spectrometer, which provided simultaneous very high-resolution (VHR) visible imagery with approximately 60 cm ground pixel resolution during this study. The survey domains are illustrated in Figure 12.

The ANG instrument was flown at approximately 8 km altitude (above ground level) for

22 days between September 22nd and October 25th. It repeatedly surveyed subsections of the Delaware and Midland basins, areas with dense Oil and Gas activity (indicated by the darker red region in Figure 12). GAO, deployed at approximately 4.5 km altitude, surveyed the extensive Permian (Delaware + Midland basins) over 21 flight days from October 10th to November 4th (black boxes in Figure 12A). The GAO flight boxes were designed to map the entire study domain once, capturing as much O&G infrastructure as possible, and overlapped with the AVIRIS-NG areas. The 4.5 km and 8 km flight altitudes of GAO and ANG allow for 4.5 m and 8 m ground pixel resolutions, respectively.

The two instruments measure ground-reflected backscattered solar radiance from 380 nm to 2510 nm at a 5 nm spectral resolution, allowing for methane slant column retrievals around the 2300 nm methane absorption feature. Flights were performed between 15:00 to 20:00 UTC (10:00-15:00 local time) to maximize solar light. The matched-filter method was employed to retrieve methane enhancement from the observed solar backscatter spectrum[3,83]. The observed spectrum is fitted to a background spectrum convolved with a target methane absorption spectrum, capturing the 2.3 μm absorption band. The method directly retrieves the methane enhancement above the background. All methane plumes from the instruments were determined visually using the retrieved methane maps. For classification as a plume, methane enhancements must have a spatial plume structure that is distinct from surface spectroscopy identifiable in the imaging spectrometer's RGB layers. The spatial extent of each plume was determined by extending radially outward from the origin of the plume and quantifying the maximum distance where significant methane was still detected above a 1000 ppm-m threshold. A maximum merge distance of 20 m was allowed between gaps in a plume, while a maximum distance threshold of 150 m was set for the plume's spatial extent. The plume locations are given in Figure 12. The plume emission rate was determined using the integrated mass enhancement method from Duren et al.[32].

We excluded a few GAO flight lines from the analysis due to geolocation errors caused by poor orthorectification. These flight track lines, observed on 2019-10-13, 2019-10-16, and

2019-10-17, had lower plume counts than other tracks observing similar emissions activity areas. The excluded flight lines and corresponding plume detections are marked in gray in Figure 12.

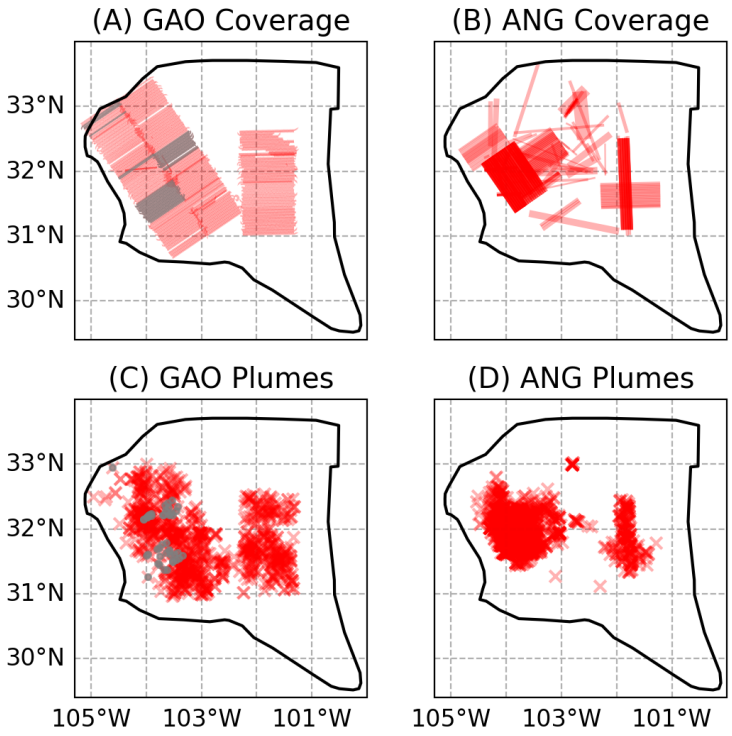

Figure 12: Spatial coverage and plume detection locations of ANG and GAO instruments for the Fall 2019 Carbon Mapper survey in the Permian Basin. The thick black contour marks the geological extent of the Permian Basin. Panels (A) and (B) show the coverage of GAO and ANG instruments, respectively, while Panels (C) and (D) display the plume detection locations for each instrument. The darker red regions indicate multiple overpasses in Panels (A) and (B). Poor performance of several GAO lines due to geolocation errors led to their exclusion from our analysis (marked in gray in the respective panels). The survey targeted two major hotspots of oil and gas activity in the Permian: the Delaware (West) and Midland (East) basins.

References

(1) Brandt, A. R. et al. Methane leaks from North American natural gas systems. *Science (80-.).* **2014**, *343*, 733–735.

(2) Kort, E. A.; Frankenberg, C.; Costigan, K. R.; Lindenmaier, R.; Dubey, M. K.;

Wunch, D. Four corners: The largest US methane anomaly viewed from space. *Geophys. Res. Lett.* **2014**, *41*, 6898–6903.

(3) Frankenberg, C.; Thorpe, A. K.; Thompson, D. R.; Hulley, G.; Kort, E. A.; Vance, N.; Borchardt, J.; Krings, T.; Gerilowski, K.; Sweeney, C.; Conley, S.; Bue, B. D.; Aubrey, A. D.; Hook, S.; Green, R. O. Airborne methane remote measurements reveal heavy-tail flux distribution in Four Corners region. *Proc. Natl. Acad. Sci.* **2016**, *113*, 9734–9739.

(4) Conley, S.; Franco, G.; Faloona, I.; Blake, D. R.; Peischl, J.; Ryerson, T. B. Methane emissions from the 2015 Aliso Canyon blowout in Los Angeles, CA. *Science (80-.).* **2016**, *351*, 1317–1320.

(5) Zavala-Araiza, D.; Alvarez, R. A.; Lyon, D. R.; Allen, D. T.; Marchese, A. J.; Zimmerle, D. J.; Hamburg, S. P. Super-emitters in natural gas infrastructure are caused by abnormal process conditions. *Nat. Commun.* **2017**, *8*.

(6) Alvarez, R. A. et al. Assessment of Methane Emissions from the U.S. Oil and Gas Supply Chain. *Sci. (in Rev.* **2018**, *7204*, 1–9.

(7) Maasakkers, J. D.; Varon, D. J.; Elfarsdóttir, A.; McKeever, J.; Jervis, D.; Mahapatra, G.; Pandey, S.; Lorente, A.; Borsdorff, T.; Foorthuis, L. R.; Schuit, B. J.; Tol, P.; van Kempen, T. A.; van Hees, R.; Aben, I. Using satellites to uncover large methane emissions from landfills. *Sci. Adv.* **2022**, *8*, 1–9.

(8) Sherwin, E. D.; Rutherford, J. S.; Zhang, Z.; Chen, Y.; Wetherley, E. B.; Yakovlev, P. V.; Berman, E. S. F.; Jones, B. B.; Cusworth, D. H.; Thorpe, A. K.; Ayasse, A. K.; Duren, R. M.; Brandt, A. R. US oil and gas system emissions from nearly one million aerial site measurements. **2024**, *627*.

(9) Varon, D. J. et al. Continuous weekly monitoring of methane emissions from the Per-

mian Basin by inversion of TROPOMI satellite observations. *Atmos. Chem. Phys.* **2023**, *23*, 7503–7520.

(10) Pandey, S.; Gautam, R.; Houweling, S.; Van Der Gon, H. D.; Sadavarte, P.; Borsdorff, T.; Hasekamp, O.; Landgraf, J.; Tol, P.; Van Kempen, T.; Hoogeveen, R.; Van Hees, R.; Hamburg, S. P.; Maasakkers, J. D.; Aben, I. Satellite observations reveal extreme methane leakage from a natural gas well blowout. *Proc. Natl. Acad. Sci. U. S. A.* **2019**, *116*, 26376–26381.

(11) Lauvaux, T.; Giron, C.; Mazzolini, M.; D'Aspremont, A.; Duren, R.; Cusworth, D.; Shindell, D.; Ciais, P. Global assessment of oil and gas methane ultra-emitters. *Science (80-.).* **2022**, *375*, 557–561.

(12) Cusworth, D. H. et al. Quantifying methane emissions from United States landfills. *Science (80-.).* **2024**, *383*, 1499–1504.

(13) Nisbet, E. G. et al. Very Strong Atmospheric Methane Growth in the 4 Years 2014–2017: Implications for the Paris Agreement. *Global Biogeochem. Cycles* **2019**, *33*, 318–342.

(14) Ocko, I. B.; Sun, T.; Shindell, D.; Oppenheimer, M.; Hristov, A. N.; Pacala, S. W.; Mauzerall, D. L.; Xu, Y.; Hamburg, S. P. Acting rapidly to deploy readily available methane mitigation measures by sector can immediately slow global warming. *Environ. Res. Lett.* **2021**, *16*.

(15) UNEP International Methane Emissions Observatory. `https://www.unep.org/explore-topics/energy/what-we-do/methane/imeohttps://ec.europa.eu/commission/presscorner/detail/en/IP{\_}21{\_}5636`.

(16) Janssens-Maenhout, G. et al. EDGAR v4.3.2 Global Atlas of the three major greenhouse gas emissions for the period 1970-2012. *Earth Syst. Sci. Data* **2019**, *11*, 959–1002.

(17) Maasakkers, J. D.; Jacob, D. J.; Sulprizio, M. P.; Turner, A. J.; Weitz, M.; Wirth, T.; Hight, C.; DeFigueiredo, M.; Desai, M.; Schmeltz, R.; Hockstad, L.; Bloom, A. A.; Bowman, K. W.; Jeong, S.; Fischer, M. L. Gridded National Inventory of U.S. Methane Emissions. *Environ. Sci. Technol.* **2016**, *50*, 13123–13133.

(18) Houweling, S.; Kaminski, T.; Dentener, F.; Lelieveld, J.; Heimann, M. Inverse modeling of methane sources and sinks using the adjoint of a global transport model. *J. Geophys. Res.* **1999**, *104*, 26137–26160.

(19) Bergamaschi, P.; Frankenberg, C. Inverse modeling of global and regional CH$_4$ emissions using SCIAMACHY satellite retrievals. *J. Geophys. Res.* **2009**, *114*, 1–28.

(20) Monteil, G.; Houweling, S.; Butz, A.; Guerlet, S.; Schepers, D.; Hasekamp, O.; Frankenberg, C.; Scheepmaker, R.; Aben, I.; Röckmann, T. Comparison of CH$_4$ inversions based on 15 months of GOSAT and SCIAMACHY observations. *J. Geophys. Res. Atmos.* **2013**, *118*, 11,807–11,823.

(21) Miller, S. M.; Wofsy, S. C.; Michalak, A. M.; Kort, E. A.; Andrews, A. E.; Biraud, S. C.; Dlugokencky, E. J.; Eluszkiewicz, J.; Fischer, M. L.; Janssens-Maenhout, G.; Miller, B. R.; Miller, J. B.; Montzka, S. A.; Nehrkorn, T.; Sweeney, C. Anthropogenic emissions of methane in the United States. *Proc. Natl. Acad. Sci. U. S. A.* **2013**, *110*, 20018–20022.

(22) Pandey, S.; Houweling, S.; Krol, M.; Aben, I.; Chevallier, F.; Dlugokencky, E. J.; Gatti, L. V.; Gloor, E.; Miller, J. B.; Detmers, R.; Machida, T.; Röckmann, T. Inverse modeling of GOSAT-retrieved ratios of total column CH$_4$ and CO$_2$ for 2009 and 2010. *Atmos. Chem. Phys.* **2016**, *16*, 5043–5062.

(23) Zhang, Y.; J. Jacob, D.; Lu, X.; D. Maasakkers, J.; R. Scarpelli, T.; Sheng, J. X.; Shen, L.; Qu, Z.; P. Sulprizio, M.; Chang, J.; Anthony Bloom, A.; Ma, S.; Worden, J.; J. Parker, R.; Boesch, H. Attribution of the accelerating increase in atmospheric methane

during 2010-2018 by inverse analysis of GOSAT observations. *Atmos. Chem. Phys.* **2021**, *21*, 3643–3666.

(24) Worden, J. R.; Cusworth, D. H.; Qu, Z.; Yin, Y.; Zhang, Y.; Bloom, A. A.; Ma, S.; Byrne, B. K.; Scarpelli, T.; Maasakkers, J. D.; Crisp, D.; Duren, R.; Jacob, D. J. The 2019 methane budget and uncertainties at 1° resolution and each country through Bayesian integration Of GOSAT total column methane data and a priori inventory estimates. *Atmos. Chem. Phys.* **2022**, *22*, 6811–6841.

(25) Basu, S.; Baker, D. F.; Chevallier, F.; Patra, P. K.; Liu, J.; Miller, J. B. The impact of transport model differences on CO 2 surface flux estimates from OCO-2 retrievals of column average CO 2. **2018**, 7189–7215.

(26) Houweling, S.; Krol, M.; Bergamaschi, P.; Frankenberg, C.; Dlugokencky, E. J.; Morino, I.; Notholt, J.; Sherlock, V.; Wunch, D.; Beck, V.; Gerbig, C.; Chen, H.; Kort, E. A.; Röckmann, T.; Aben, I. A multi-year methane inversion using SCIAMACHY, accounting for systematic errors using TCCON measurements. *Atmos. Chem. Phys.* **2014**, *14*, 3991–4012.

(27) Schuh, A. E.; Byrne, B.; Jacobson, A. R.; Crowell, S. M.; Deng, F.; Baker, D. F.; Johnson, M. S.; Philip, S.; Weir, B. On the role of atmospheric model transport uncertainty in estimating the Chinese land carbon sink. *Nature* **2022**, *603*, E13–E14.

(28) Balasus, N.; Jacob, D. J.; Lorente, A.; Maasakkers, J. D.; Parker, R. J.; Boesch, H.; Chen, Z.; Kelp, M. M.; Nesser, H.; Varon, D. J. A blended TROPOMI+GOSAT satellite data product for atmospheric methane using machine learning to correct retrieval biases. *Atmos. Meas. Tech.* **2023**, *16*, 3787–3807.

(29) Lorente, A.; Borsdorff, T.; Martinez-velarte, M. C.; Landgraf, J. Accounting for surface reflectance spectral features in TROPOMI methane retrievals. **2022**, *2017*, 1–15.

(30) Kunkel, W. M.; Carre-Burritt, A. E.; Aivazian, G. S.; Snow, N. C.; Harris, J. T.; Mueller, T. S.; Roos, P. A.; Thorpe, M. J. Extension of Methane Emission Rate Distribution for Permian Basin Oil and Gas Production Infrastructure by Aerial LiDAR. *EarthArXiv* **2023**,

(31) Jervis, D.; McKeever, J.; Durak, B. O.; Sloan, J. J.; Gains, D.; Varon, D. J.; Ramier, A.; Strupler, M.; Tarrant, E. The GHGSat-D imaging spectrometer. *Atmos. Meas. Tech.* **2021**, *14*, 2127–2140.

(32) Duren, R. M. et al. California ' s methane super-emitters. *Nature* **2019**, *575*, 180–184.

(33) Guanter, L.; Irakulis-Loitxate, I.; Gorroño, J.; Sánchez-García, E.; Cusworth, D. H.; Varon, D. J.; Cogliati, S.; Colombo, R. Mapping methane point emissions with the PRISMA spaceborne imaging spectrometer. *Remote Sens. Environ.* **2021**, *265*, 112671.

(34) Varon, D. J.; Jervis, D.; McKeever, J.; Spence, I.; Gains, D.; Jacob, D. J. High-frequency monitoring of anomalous methane point sources with multispectral Sentinel-2 satellite observations. *Atmos. Meas. Tech.* **2021**, *14*, 2771–2785.

(35) Cusworth, D. H.; Thorpe, A. K.; Ayasse, A. K.; Stepp, D.; Heckler, J.; Asner, G. P.; Miller, C. E.; Yadav, V.; Chapman, J. W.; Eastwood, M. L.; Green, R. O.; Hmiel, B.; Lyon, D. R.; Duren, R. M. Strong methane point sources contribute a disproportionate fraction of total emissions across multiple basins in the United States. *Proc. Natl. Acad. Sci. U. S. A.* **2022**, *119*, 1–7.

(36) Chen, Y.; Sherwin, E. D.; Berman, E. S.; Jones, B. B.; Gordon, M. P.; Wetherley, E. B.; Kort, E. A.; Brandt, A. R. Quantifying Regional Methane Emissions in the New Mexico Permian Basin with a Comprehensive Aerial Survey. *Environ. Sci. Technol.* **2022**, *56*, 4317–4323.

(37) Johnson, M. R.; Conrad, B. M.; Tyner, D. R. Creating measurement-based oil and

gas sector methane inventories using source-resolved aerial surveys. *Commun. Earth Environ.* **2023**, *4*, 1–9.

(38) Rutherford, J. S.; Sherwin, E. D.; Ravikumar, A. P.; Heath, G. A.; Englander, J.; Cooley, D.; Lyon, D.; Omara, M.; Langfitt, Q.; Brandt, A. R. Closing the methane gap in US oil and natural gas production emissions inventories. *Nat. Commun.* **2021**, *12*, 1–12.

(39) Lyon, D. R.; Zavala-Araiza, D.; Alvarez, R. A.; Harriss, R.; Palacios, V.; Lan, X.; Talbot, R.; Lavoie, T.; Shepson, P.; Yacovitch, T. I.; Herndon, S. C.; Marchese, A. J.; Zimmerle, D.; Robinson, A. L.; Hamburg, S. P. Constructing a Spatially Resolved Methane Emission Inventory for the Barnett Shale Region. *Environ. Sci. Technol.* **2015**, *49*, 8147–8157.

(40) Naus, S.; Maasakkers, J. D.; Gautam, R.; Omara, M.; Stikker, R.; Veenstra, A. K.; Nathan, B.; Irakulis-Loitxate, I.; Guanter, L.; Pandey, S.; Girard, M.; Lorente, A.; Borsdorff, T.; Aben, I. Assessing the Relative Importance of Satellite-Detected Methane Superemitters in Quantifying Total Emissions for Oil and Gas Production Areas in Algeria. *Environ. Sci. Technol.* **2023**,

(41) Xia, H.; Strayer, A.; Ravikumar, A. P. The role of emission size distribution on the efficacy of new technologies to reduce methane emissions from the oil and gas sector. *Environ. Sci. Technol.* **2024**, *58*, 1088–1096.

(42) Zimmerle, D.; Vaughn, T.; Bell, C.; Bennett, K.; Deshmukh, P.; Thoma, E. Detection Limits of Optical Gas Imaging for Natural Gas Leak Detection in Realistic Controlled Conditions. *Environ. Sci. Technol.* **2020**, *54*, 11506–11514.

(43) Zavala-Araiza, D.; Alvarez, R. A.; Lyon, D. R.; Allen, D. T.; Marchese, A. J.; Zimmerle, D. J.; Hamburg, S. P. Super-emitters in natural gas infrastructure are caused by abnormal process conditions. *Nat. Commun.* **2017**, *8*.

(44) Omara, M.; Zimmerman, N.; Sullivan, M. R.; Li, X.; Ellis, A.; Cesa, R.; Subramanian, R.; Presto, A. A.; Robinson, A. L. Methane emissions from natural gas production sites in the United States: Data synthesis and national estimate. *Environ. Sci. Technol.* **2018**, acs.est.8b03535.

(45) Berman, E. S. F.; Wetherley, E. B.; Jones, B. B. Kairos Aerospace: Technical White Paper: Methane Detection.

(46) Irakulis-loitxate, A. I.; Guanter, L.; Maasakkers, J. D.; Zavala, D. Satellites unveil easily-fixable super-emissions in one of the world ' s largest methane hotspot regions. 1–32.

(47) Cusworth, D. H. et al. Multisatellite Imaging of a Gas Well Blowout Enables Quantification of Total Methane Emissions. *Geophys. Res. Lett.* **2021**, *48*, 1–9.

(48) Pandey, S.; Houweling, S.; Krol, M.; Aben, I. Influence of Atmospheric Transport on Estimates of Variability in the Global Methane Burden Geophysical Research Letters. *Geophys. Res. Lett.* **2019**, *46*, 2302–2311.

(49) Varon, D. J.; McKeever, J.; Jervis, D.; Maasakkers, J. D.; Pandey, S.; Houweling, S.; Aben, I.; Scarpelli, T.; Jacob, D. J. Satellite Discovery of Anomalously Large Methane Point Sources From Oil/Gas Production. *Geophys. Res. Lett.* **2019**, *46*, 13507–13516.

(50) Maasakkers, J. D.; Omara, M.; Gautam, R.; Lorente, A.; Pandey, S.; Tol, P.; Borsdorff, T.; Houweling, S.; Aben, I. Reconstructing and quantifying methane emissions from the full duration of a 38-day natural gas well blowout using space-based observations. *Remote Sens. Environ.* **2022**, *270*, 112755.

(51) Pandey, S.; van Nistelrooij, M.; Maasakkers, J. D.; Sutar, P.; Houweling, S.; Varon, D. J.; Tol, P.; Gains, D.; Worden, J.; Aben, I. Daily detection and quantification of methane leaks using Sentinel-3: a tiered satellite observation approach with Sentinel-2 and Sentinel-5p. *Remote Sens. Environ.* **2023**, *296*, 113716.

(52) Sánchez-García, E.; Gorroño, J.; Irakulis-Loitxate, I.; Varon, D. J.; Guanter, L. Mapping methane plumes at very high spatial resolution with the WorldView-3 satellite. *Atmos. Meas. Tech.* **2022**, *15*, 1657–1674.

(53) Ehret, T.; De Truchis, A.; Mazzolini, M.; Morel, J. M.; D'Aspremont, A.; Lauvaux, T.; Duren, R.; Cusworth, D.; Facciolo, G. Global Tracking and Quantification of Oil and Gas Methane Emissions from Recurrent Sentinel-2 Imagery. *Environ. Sci. Technol.* **2022**, *56*, 10517–10529.

(54) Jacob, D. J.; Varon, D. J.; Cusworth, D. H.; Dennison, P. E.; Frankenberg, C.; Gautam, R.; Guanter, L.; Kelley, J.; Mckeever, J.; Ott, L. E.; Poulter, B.; Qu, Z.; Thorpe, A. K.; Worden, J. R.; Duren, R. M. Quantifying methane emissions from the global scale down to point sources using satellite observations of atmospheric methane. *Atmos. Chem. Phys.* **2022**, 9617–9646.

(55) Cusworth, D. H.; Bloom, A. A.; Ma, S.; Miller, C. E.; Bowman, K.; Yin, Y.; Maasakkers, J. D.; Zhang, Y.; Scarpelli, T. R.; Qu, Z.; Jacob, D. J.; Worden, J. R. A Bayesian framework for deriving sector-based methane emissions from top-down fluxes. *Commun. Earth Environ.* **2021**, *2*, 1–8.

(56) Schuit, B. J. et al. Automated detection and monitoring of methane super-emitters using satellite data. *Atmos. Chem. Phys. Discuss.* **2023**, 1–47.

(57) Thorpe, A. K. et al. Mapping methane concentrations from a controlled release experiment using the next generation airborne visible/infrared imaging spectrometer (AVIRIS-NG). *Remote Sens. Environ.* **2016**, *179*, 104–115.

(58) Conrad, B. M.; Tyner, D. R.; Johnson, M. R. Robust probabilities of detection and quantification uncertainty for aerial methane detection: Examples for three airborne technologies. *Remote Sens. Environ.* **2023**, *288*, 113499.

(59) Vaughn, T. L.; Bell, C. S.; Pickering, C. K.; Schwietzke, S.; Heath, G. A.; Pétron, G.; Zimmerle, D. J.; Schnell, R. C.; Nummedal, D. Temporal variability largely explains top-down/bottom-up difference in methane emission estimates from a natural gas production region. *Proc. Natl. Acad. Sci. U. S. A.* **2018**, *115*, 11712–11717.

(60) Allen, D. T.; Cardoso-Saldaña, F. J.; Kimura, Y. Variability in Spatially and Temporally Resolved Emissions and Hydrocarbon Source Fingerprints for Oil and Gas Sources in Shale Gas Production Regions. *Environ. Sci. Technol.* **2017**, *51*, 12016–12026.

(61) Nesser, H.; Jacob, D. J.; Maasakkers, J. D.; Lorente, A.; Chen, Z.; Lu, X.; Shen, L.; Qu, Z.; Sulprizio, M. P.; Winter, M.; Ma, S.; Anthony Bloom, A.; Worden, R.; Stavins, R. N.; Randles, C. A. High-resolution U.S. methane emissions inferred from an inversion of 2019 TROPOMI satellite data: contributions from individual states, urban areas, and landfills. *Acpd* **2023**,

(62) Turner, A. J. et al. Estimating global and North American methane emissions with high spatial resolution using GOSAT satellite data. *Atmos. Chem. Phys.* **2015**, *15*, 7049–7069.

(63) Maasakkers, J. D.; McDuffie, E. E.; Sulprizio, M. P.; Chen, C.; Schultz, M.; Brunelle, L.; Thrush, R.; Steller, J.; Sherry, C.; Jacob, D. J.; Jeong, S.; Irving, B.; Weitz, M. A Gridded Inventory of Annual 2012-2018 U.S. Anthropogenic Methane Emissions. *Environ. Sci. Technol.* **2023**, *57*, 16276–16288.

(64) Jacob, D. J.; Turner, A. J.; Maasakkers, J. D.; Sheng, J.; Sun, K.; Liu, X.; Chance, K.; Aben, I.; McKeever, J.; Frankenberg, C. Satellite observations of atmospheric methane and their value for quantifying methane emissions. *Atmos. Chem. Phys.* **2016**, *16*, 14371–14396.

(65) Buchwitz, M.; Schneising, O.; Reuter, M.; Heymann, J.; Krautwurst, S.; Bovensmann, H.; Burrows, J. P.; Boesch, H.; Parker, R. J.; Detmers, R. G.; Hasekamp, O. P.;

Aben, I.; Butz, A.; Frankenberg, C. Satellite-derived methane hotspot emission estimates using a fast data-driven method. *Atmos. Chem. Phys. Discuss.* **2016**, 1–40.

(66) Pandey, S.; Houweling, S.; Lorente, A.; Borsdorff, T.; Tsivlidou, M.; Anthony Bloom, A.; Poulter, B.; Zhang, Z.; Aben, I. Using satellite data to identify the methane emission controls of South Sudan's wetlands. *Biogeosciences* **2021**, *18*, 557–572.

(67) Feldman, A. F.; Zhang, Z.; Yoshida, Y.; Chatterjee, A.; Poulter, B. Using OCO-2 column CO 2 retrievals to rapidly detect and estimate biospheric surface carbon flux anomalies. **2023**, 1545–1563.

(68) Cusworth, D. H.; Duren, R. M.; Thorpe, A. K.; Olson-Duvall, W.; Heckler, J.; Chapman, J. W.; Eastwood, M. L.; Helmlinger, M. C.; Green, R. O.; Asner, G. P.; Dennison, P. E.; Miller, C. E. Intermittency of Large Methane Emitters in the Permian Basin. *Environ. Sci. Technol. Lett.* **2021**,

(69) Zhang, Y. et al. Quantifying methane emissions from the largest oil-producing basin in the United States from space. *Sci. Adv.* **2020**, *2007*, 1–10.

(70) Irakulis-Loitxate, I.; Guanter, L.; Maasakkers, J. D.; Zavala-Araiza, D.; Aben, I. Satellites Detect Abatable Super-Emissions in One of the World's Largest Methane Hotspot Regions. *Environ. Sci. Technol.* **2022**, *56*, 2143–2152.

(71) Lauvaux, T.; Giron, C.; Mazzolini, M.; D'Aspremont, A.; Duren, R.; Cusworth, D.; Shindell, D.; Ciais, P. Global assessment of oil and gas methane ultra-emitters. *Science (80-.).* **2022**, *375*, 557–561.

(72) United Nations Environment Programme (UNEP) Methane Alert and Response System (MARS). \url{https://methanedata.unep.org/plumemap?mars=false}, 2023; `https://methanedata.unep.org/plumemap?mars=false`.

(73) Zavala-Araiza, D. et al. Reconciling divergent estimates of oil and gas methane emissions. *Proc. Natl. Acad. Sci. U. S. A.* **2015**, *112*, 15597–15602.

(74) Allen, D. T.; Torres, V. M.; Thomas, J.; Sullivan, D. W.; Harrison, M.; Hendler, A.; Herndon, S. C.; Kolb, C. E.; Fraser, M. P.; Hill, A. D.; Lamb, B. K.; Miskimins, J.; Sawyer, R. F.; Seinfeld, J. H. Measurements of methane emissions at natural gas production sites in the United States. *Proceedings of the National Academy of Sciences* **2013**, *110*, 17768–17773.

(75) Omara, M.; Himmelberger, A.; Mackay, K.; Williams, J. P.; Benmergui, J.; Sargent, M.; Wofsy, S. C.; Gautam, R. Constructing a measurement-based spatially explicit inventory of US oil and gas methane emissions. **2024**, 1–25.

(76) Hamburg, S.; Gautam, R.; Zavala-Araiza, D. MethaneSAT - A New Tool Purpose-Built to Measure Oil and Gas Methane Emissions from Space. 2022; `https://doi.org/10.2118/210922-MS`.

(77) NASA New Proposals to Help NASA Advance Knowledge of Our Changing Climate. \url{https://www.nasa.gov/news-release/new-proposals-to-help-nasa-advance-knowledge-of-our-changing-climate/}, 2024.

(78) Cusworth, D. H.; Thorpe, A. K.; Miller, C. E.; Ayasse, A. K.; Jiorle, R.; Duren, R. M.; Nassar, R.; Mastrogiacomo, J.-P.; Nelson, R. R. Two years of satellite-based carbon dioxide emission quantification at the world's largest coal-fired power plants. *Atmos. Chem. Phys.* **2023**, *23*, 14577–14591.

(79) Varon, D. J.; Jervis, D.; Pandey, S.; Gallardo, S. L.; Balasus, N.; Yang, L. H.; Jacob, D. J. Quantifying NO_x point sources with Landsat and Sentinel-2 satellite observations of NO₂ plumes. *Proc. Natl. Acad. Sci.* **2024**, *121*, e2317077121.

(80) Thorpe, A. K. et al. Attribution of individual methane and carbon dioxide emission sources using EMIT observations from space. *Sci. Adv.* **2023**, *9*, 1–13.

(81) Lorenc, A. C. Analysis methods for numerical weather prediction. *Q. J. R. Meteorol. Soc.* **1986**, *112*, 1177–1194.

(82) Brasseur, G. P.; Jacob, D. J. *Model. Atmos. Chem.*; 2017.

(83) Thompson, D. R.; Thorpe, A. K.; Frankenberg, C.; Green, R. O.; Duren, R.; Guanter, L.; Hollstein, A.; Middleton, E.; Ong, L.; Ungar, S. Space-based remote imaging spectroscopy of the Aliso Canyon CH4superemitter. *Geophys. Res. Lett.* **2016**,